

1. Introduction

Bacteria play a prominent role in many ecosystems, including aquatic environments such as lakes and oceans (del Giorgio and Duarte, 2002; Hart et al., 2000; Biddanda and Cotner, 2002; Stocker and Seymour, 2012). In the oceans, bacteria act as recyclers by consuming dissolved organic matter (DOM) and making this material available to higher trophic levels (Azam and Malfatti, 2007). In coastal seas and lakes, bacteria populations can deplete dissolved oxygen, leading to the formation of anoxic waters (Diaz and Rosenberg, 2008). Bacteria are also widely used in industry in bioreactors for diverse applications such as wastewater treatment (Baird and Smith, 2002), biofuel production (Schenk et al., 2008), and medicine production (Marwick et al., 1999).

In all these examples, bacteria exist in turbulent aqueous environments. Yet, the interaction between turbulence and microbiological organisms has received little attention. At the scale of a single bacterium, the uptake of dissolved nutrients by the cell is partly dictated by the diffusive transport of molecules towards the cell surface. Due to the small size of bacterial cells, it is thought that this process is not directly influenced by turbulence (Lazier and Mann, 1989; Karp-Boss et al., 1996). However, recent studies have shown that while not impacting uptake at a bacterium scale, turbulence does affect bacterial respiration and growth at a population scale, both on long time scales (Arin et al., 2002; Bergstedt et al., 2004; Al-Homoud et al., 2007) and short time scales (Munoz-Garcia et al., 2010; Taylor and Stocker, 2012).

Some bacteria have evolved the ability to swim using rotating flagella (Brennen and Winet, 1977; Lauga and Powers, 2009). Bacteria motion can be modelled as a “random walk” with successions of straight runs and tumblings dictated by the direction of the rotation of flagella. By adjusting their tumbling rates, motile bacteria use a biased random walk in order to favour a direction in response to certain stimuli, whether attractant or repellent. Strategies for motility are classified based on the stimulus and include phototaxis for the response to light (Engelmann, 1883), thermotaxis for the response to temperature (Paster and Ryu, 2008), and chemotaxis for the response to chemical cues (Berg, 1983). Chemotaxis is widespread in marine ecosystems and is believed to be an important factor in the ocean's biogeochemical cycles (Azam and Malfatti, 2007; Guasto et al., 2012). Motile marine bacteria use chemotaxis as a foraging strategy to rapidly respond to ephemeral patches of nutrients (Stocker et al., 2008).

Recently, Taylor and Stocker (2012) used DNS to show that turbulence can influence the rate at which a population of chemotactic bacteria consumes dissolved nutrients. In a turbulent environment, patches of dissolved nutrients are stirred into a network of thin filaments. Through chemotaxis, motile bacteria cluster near the centre of the nutrient-rich filaments, thereby delivering an advantage to motile bacteria relative to their non-motile counterparts. Results of DNS showed that the benefit conferred by chemotaxis in a turbulent environment is subject to a series of trade-offs which depend on the ratio of timescales associated with chemotaxis, uptake, and turbulent mixing. They found that the chemotactic advantage was generally largest for moderate turbulence intensities, where turbulence was strong enough to quickly stir a nutrient patch into thin filaments, but not so strong as to homogenize the patch before it could be exploited by motile bacteria.

The work of Taylor and Stocker (2012) focused primarily on the influence of the level of turbulence and the bacteria swimming speed on the chemotactic advantage. Here, we extend their results by examining a wider range of physical and biological factors. By systematically varying the parameters associated to each feature in a suite of numerical simulations, we find that the uptake

advantage gained through chemotaxis can be highly sensitive to environmental conditions and biological parameters, including patch size, solute diffusivity, chemotactic efficiency, and Reynolds number. The rest of the paper is organized as follows. A brief description of the methodology along with the model equations are presented in Section 2. Results from the numerical simulations are presented in Sections 3 and 4, with an emphasis on the time-dependent uptake advantage due to chemotaxis and the time-integrated chemotactic advantage. Finally, results are discussed and conclusions are offered in Section 5.

2. Methodology

We have conducted a series of controlled direct numerical simulations (DNS) starting with a baseline case. In each simulation set, we explore the sensitivity of the uptake rate with respect to a physical characteristic of the fluid flow or a feature of the biological response. From this, we draw a comprehensive picture of how the chemotactic bacteria population responds to changing environmental conditions. By definition a DNS resolves all scales of variability in the flow and scalar fields. While this places restrictions on the size of the domain that can be considered and makes the simulations computationally expensive, it removes any dependence on sub-grid scale or turbulence models.

Here, we model a three-dimensional, statistically steady, homogeneous, isotropic turbulent flow. Details of the flow equations are given in Appendix A.1. A continuum approach is used here for modelling the concentrations of dissolved nutrients N along with two populations of motile bacteria B_M and non-motile bacteria B_{NM} , as in Taylor and Stocker (2012), using the following equations (given in their dimensional form):

$$\frac{\partial N}{\partial t} + \mathbf{u} \cdot \nabla N = -\frac{N}{\tau_U} - \frac{B_M}{B_{NM}} \frac{N}{\tau_U} + \kappa_N \nabla^2 N, \quad (1a)$$

$$\frac{\partial B_M}{\partial t} + \mathbf{u} \cdot \nabla B_M = -\nabla \cdot (B_M \mathbf{V}_C) + \kappa_B \nabla^2 B_M, \quad (1b)$$

$$\frac{\partial B_{NM}}{\partial t} + \mathbf{u} \cdot \nabla B_{NM} = 0. \quad (1c)$$

All fields are advected by the fluid velocity, \mathbf{u} . Dissolved nutrients and motile bacteria diffuse with a diffusivity given by κ_N and κ_B , respectively. Both motile and non-motile bacteria populations consume nutrients. On the scale of a bacterium, the fluid flow is entirely laminar, and transport of nutrient due to advection is negligible compare to diffusion (Karp-Boss et al., 1996) (see Appendix A.2 for more details). Hence the bacteria uptake timescale, τ_U , is determined by considering continuous absorption of nutrients by diffusion through the surface of a sphere, assuming that bacteria act as perfect absorbers, i.e. the local nutrient concentration on the bacterium membrane is zero, and uptake is diffusion-limited (Kiorboe, 2008)

$$\tau_{U_{NM}} = (2\pi a \kappa_N B_{NM})^{-1} = \tau_U; \tau_{U_M} = (2\pi a \kappa_N B_M)^{-1} = \frac{B_{NM}}{B_M} \tau_U, \quad (2)$$

where a is the diameter of the bacterium, and is considered the same for both populations. The timescale τ_U is assumed to be independent of the physical environment.

The concentration of motile and non-motile bacteria is taken to be uniform at the start of each simulation. Since the advection of non-motile bacteria, $\mathbf{u} \cdot \nabla B_{NM}$, is zero initially, and there is no other mechanism by which non-motile bacteria can cluster in Eq. (1c), the non-motile bacteria remain uniformly distributed at the initial concentration for all subsequent times. We therefore do not solve Eq. (1c) directly, but do account for nutrient uptake by non-motile cells. Note that while we interpret Eq. (1c) in terms of non-motile

bacteria, motile non-chemotactic bacteria would also remain uniformly distributed, and the same conclusions would apply.

Chemotaxis is modelled as the combination of a diffusion process with diffusivity κ_B , and a chemotactic velocity \mathbf{V}_C directed up the local nutrient gradient, as described by Keller and Segel (1970). Based on the model of Lovely and Dahlquist (1975) and Berg (1983), the bacteria diffusivity coefficient follows:

$$\kappa_B = \frac{V_S^2 \tau_S}{3(1-\alpha)}, \quad (3)$$

where V_S is the motile bacteria swimming speed, τ_S the mean run time between tumbles, and α is the persistence parameter i.e. the mean value of the cosine of the angle between two runs separated by a tumbling event.

Here, we follow Taylor and Stocker (2012) and calculate the instantaneous, local chemotactic velocity using the model

$$\mathbf{V}_C = V_C \tanh\left(\frac{l_S}{N_0} |\nabla N|\right) \frac{\nabla N}{|\nabla N|}. \quad (4)$$

The maximum chemotactic speed V_C is related to the swimming speed V_S through a ‘‘chemotactic efficiency’’ coefficient $V_C = \Gamma V_S$. The chemotactic sensitivity l_S/N_0 quantifies how sensitive motile bacteria are to nutrient gradients. A large chemotactic sensitivity implies that chemotaxis is triggered even in a low nutrient-gradient environment. This approach can be linked with the model of Rivero et al. (1989) and its extensions (Ford and Cummings, 1992; Chen et al., 1998; Ahmed and Stocker, 2008a), highlighting the dependence of the chemotactic saturation length l_S on various physical and physiological factors including the swimming speed V_S and the chemotactic efficiency Γ (see Appendix B). However, here, all parameters are taken to be independent in order to study each of their influence. Finally, the demographics of bacteria are neglected since the patch lifetime (minutes) is much smaller than the cellular reproduction time (hours).

The continuum approach is used here for its mathematical simplicity. A Keller–Segel approach does not track each bacterium’s position, but models the bacteria fluxes toward positive nutrient gradients, governed here by Eq. (4). One requirement of this model is that the lengthscale characterizing the mean movement of bacteria across nutrient filaments, $V_C \tau_S$, must be smaller than the lengthscale characterizing nutrient filaments, λ_N . One can therefore define the Knudsen number $\text{Kn}_M = V_C \tau_S / \lambda_N$ to measure the validity of this approximation. Note that earlier work (Taylor and Stocker, 2012) defined Kn_M using V_S rather than V_C . Both definitions give a small Kn_M in their study, but when the chemotactic efficiency Γ is small, V_C can be significantly smaller than V_S . The largest Knudsen number for our simulations is $\text{Kn}_M = 0.07$, supporting the accuracy of the continuum approach (Bearon, 2007; Taylor and Stocker, 2012) for the entire parameter regime we explore.

The setup for DNS used here is similar to that in Taylor and Stocker (2012). In a cubic domain $\mathcal{D} = L^3$, we generate a turbulent flow in a quasi-stationary state with a constant averaged dissipation rate $\varepsilon = \nu \mathbf{u} \cdot \nabla^2 \mathbf{u}$, where ν is the fluid kinematic viscosity and $\bar{\cdot}$ is the average over the numerical domain. Once the target dissipation rate $\varepsilon = \varepsilon_T$ is reached, spherical gaussian nutrient patches, of characteristic half-width σ and equi-spaced by the distance ℓ_p , are instantaneously injected. We vary each parameter of interest and study its influence on the biophysical interaction. Values of all parameters are given in Tables C1 and C2. The ratio between the domain size L , i.e. the largest scale of the turbulent flow, and the Kolmogorov scale $\eta_K \equiv (\nu^3/\varepsilon)^{1/4}$, i.e. the smallest flow scale where viscous forces dissipate kinetic energy, is kept constant. As a result, the Taylor Reynolds number Re_λ , which characterizes the intensity of turbulence, remains constant (see Appendix A for more details).

Hence, the dissipation rate is varied independently from the Taylor Reynolds number, a constraint that is discussed in Section 5.

In experiments, the Taylor microscale Reynolds number Re_λ typically varies from 20, for weakly turbulent flows, up to several thousand for highly turbulent flows (Pope, 2000). Since the computational cost of simulations with large Re_λ along with small κ_N is prohibitive, the DNS conducted here simulates a weakly turbulent flow ($Re_\lambda = 25$). However, as will be seen, it is large enough to create a network of filaments and can be used to analyse the impact of turbulence on the uptake rate. More details on the characteristics lengthscales of the system, the numerical set-up and the resolution dependencies are given in Appendix A.

3. General results

Before describing the impact of the various physical and biological factors, we discuss the phenomenology of the baseline simulation and the quantification of the uptake advantage owing to chemotaxis. The biophysical interaction arising from chemotaxis is set by a vast number of physical and biological conditions: the fluid viscosity and dissipation rate (ν, ε) for the flow field, the initial concentration, patch half-width and diffusivity (N_0, σ, κ_N) for the nutrient field, and the populations concentrations, uptake timescale, swimming speed, swim timescale, persistence angle, chemotactic efficiency and chemotactic saturation length ($B_M, B_{NM}, \tau_U, \Gamma, V_S, \tau_S, \alpha, l_S$) for the bacteria fields. Values of the baseline simulation are given in Tables C.1 and C.2. Non-motile and motile bacteria are assumed to have the same mean concentration $\overline{B_M} = \overline{B_{NM}} = B_0$, which only affects the uptake timescale τ_U .

3.1. Phenomenology of the biophysical interaction

Fig. 1 shows a series of visualizations of the nutrient and motile bacteria fields during the course of the baseline simulation. The initial condition is shown in the top row. In the second row, turbulence has begun to stir the nutrient patches and shape them into elongated sheets. Later (third row), the nutrient field becomes a tangled network of filaments. Here, stirring and diffusion compete to set the size of the nutrient filaments; while stirring enhances nutrient gradients and acts to sharpen the filaments, diffusion causes them to spread out. The combined effects of stirring and diffusion leads to mixing, which eventually erases fluctuations in the nutrient field (bottom row).

It is clear from Fig. 1 that the lengthscales associated with the nutrient field are strongly influenced by the turbulent flow and vary in time. The nutrient field evolves into a tangled network of filaments, with characteristic lengthscale $\lambda_N = (N'^2 / \overline{\nabla N} \cdot \overline{\nabla N})^{1/2}$, where $N' = N - N_0$ represents the nutrient fluctuations. As can be seen in Fig. 2, λ_N evolves in time and eventually reaches a quasi-stationary state (QSS) where stirring and diffusion balance. During the QSS, λ_N can be approximated by neglecting the uptake terms, and using the theory of passive scalars in isotropic turbulent flows, giving $\lambda_N^{\text{QSS}} = F_N \eta_N$, where F_N is the Corrsin coefficient and $\eta_N \equiv \eta_K / \text{Sc}_N^{1/2}$ is the Batchelor scale, and $\text{Sc}_N = \nu / \kappa_N$ is the Schmidt number (see details in Appendix A.2). Previous results showed that $\lambda_N^{\text{QSS}} / \eta_N \approx 4$ for simulations with $Re_\lambda = 20$ and $\text{Sc}_N = 300$ (Taylor and Stocker, 2012), which is approximately the value obtained with the Corrsin coefficient. Note, however, that F_N depends on the Taylor Reynolds number Re_λ (see Eq. (A.5)) which may be important when extrapolating results to high Reynolds number flows, as discussed in Section 5.

Before reaching the QSS, a transient regime exists where the filament lengthscale, λ_N , is influenced by the initial patch size, σ . During the transient regime, if the initial lengthscale $\lambda_N(t=0)$ is

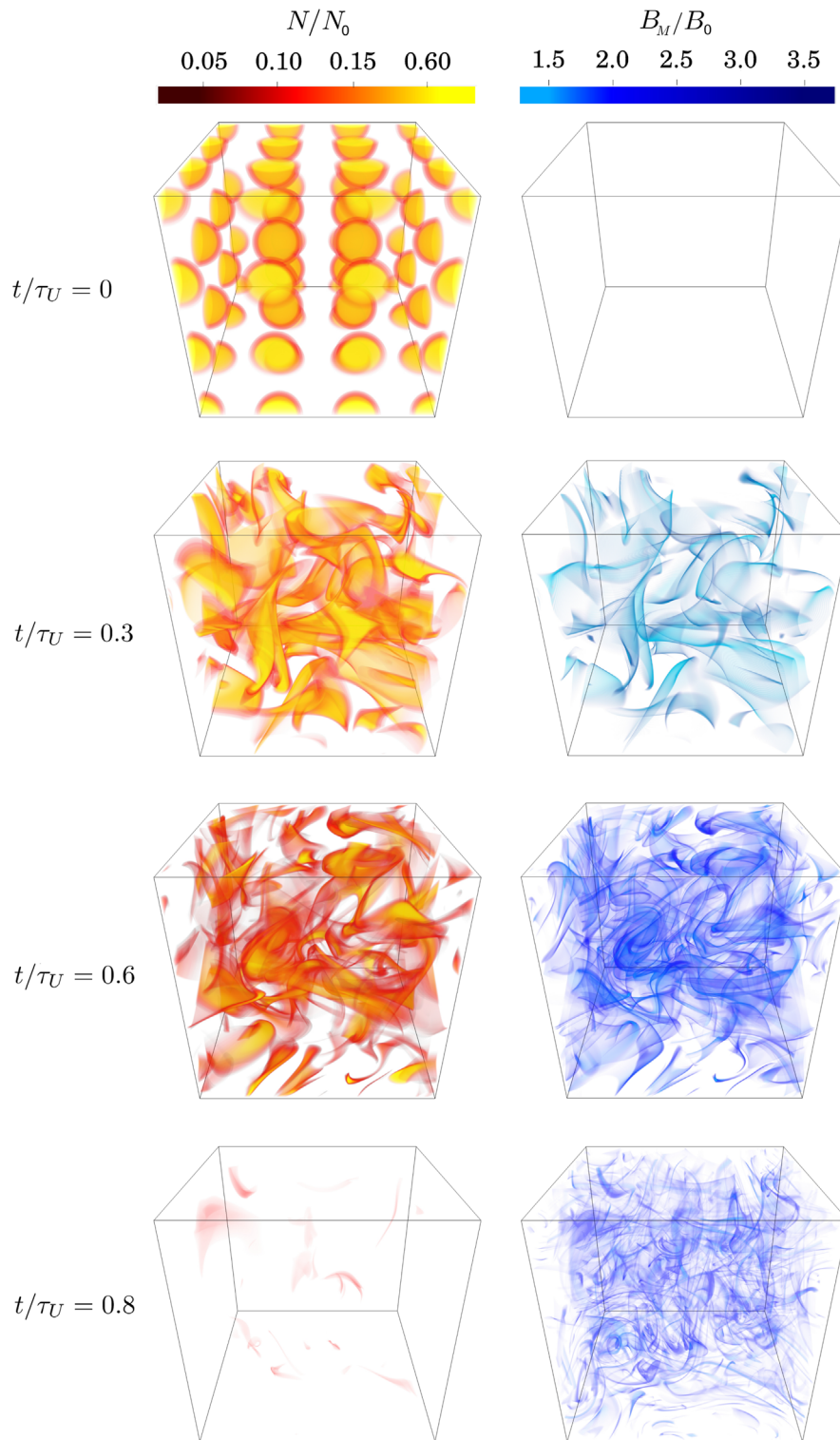


Fig. 1. Time evolution of the nutrient (left column) and motile bacteria (right column) fields for the baseline simulation ($L = 16.95$ cm, $\epsilon = 2.1 \times 10^{-8}$ m² s⁻³, $\tau_U = 160$ s and $V_C = 40$ μ ms⁻¹). Turbulence first stirs the nutrient patches into filaments until reaching a state where molecular diffusion counter-balances stirring. Filaments eventually disappear through the actions of both diffusion and uptake. Using chemotaxis, the population of motile bacteria follows rich-nutrients spots, therefore turning also into a network of thin filaments from which an uptake advantage is created. The lowest value on each color scale is made transparent and opacity increases linearly with concentration. Images made using Vapor (Clyne et al., 2007).

larger than λ_N^{QSS} , then stirring overwhelms diffusion, and λ_N decreases down to λ_N^{QSS} , which is the situation studied here. On the other hand, if $\lambda_N(t = 0)$ is smaller than λ_N^{QSS} , then we anticipate that diffusion would overwhelm stirring at early times and λ_N increases up to λ_N^{QSS} (this case is not simulated here).

As the nutrient field is stirred into a web of filaments, motile bacteria cluster around these filaments using chemotaxis (Fig. 1). The size of the resulting bacteria filaments can be characterized with the lengthscale $\lambda_B = (\overline{B'^2} / \overline{\nabla B} \cdot \overline{\nabla B})^{1/2}$, where $B' = B_M - B_0$. Through chemotaxis, λ_B reaches values smaller than λ_N (Fig. 2).

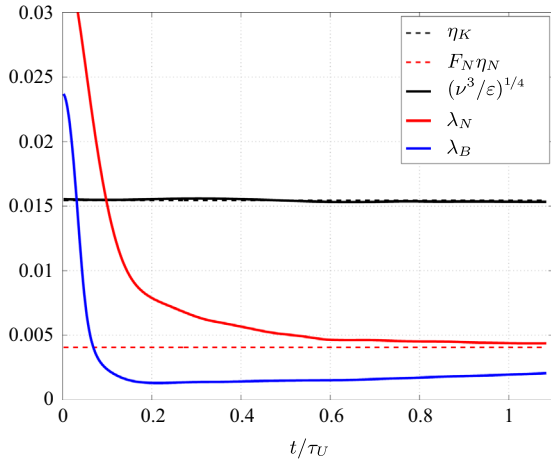


Fig. 2. Characteristic lengthscales of the system. In solid lines, the evolution in time of the lengthscales obtained from DNS with in black: the Kolmogorov scale using $\varepsilon = \nu \mathbf{u} \cdot \nabla^2 \mathbf{u}$, in red: the nutrient lengthscale λ_N , in blue: the bacteria lengthscale λ_B . The dotted lines show the analytical Kolmogorov and Batchelor–Corrsin scales, η_K and $F_N \eta_N$ respectively. (For interpretation of the references to color in this figure caption, the reader is referred to the web version of this paper.)

Once the motile bacteria concentration becomes non-uniform, it is also subject to stirring and diffusion. Finally, as nutrient fluctuations disappear, bacterial diffusivity takes over chemotaxis and the motile bacteria field relaxes toward a uniform field.

3.2. Uptake advantage rates and scaling

The uptake rate quantifies the ability of a bacteria population to absorb the surrounding nutrients. It is derived from the nutrient budget equation, Eq. (1a). Because periodic conditions are used, there is no net flux of bacteria or nutrients into the computational domain, and all terms involving the volume integral of a divergence are identically zero (applying Stokes theorem). The non-motile and motile uptake rates are therefore modelled as

$$U_{NM} = \frac{\bar{N}}{\tau_U} \quad \text{and} \quad U_M = \frac{\bar{B}_M \bar{N}}{\bar{B}_{NM} \tau_U}, \quad (5)$$

respectively.

At time t , the instantaneous uptake rate $U_M(t) + U_{NM}(t)$ is compared to the instantaneous uptake rate $2U_{NM}(t)$ without chemotaxis. Two quantities are studied, the instantaneous *chemotactic uptake advantage*

$$\Delta U(t) = U_M(t) - U_{NM}(t), \quad (6)$$

and the instantaneous *chemotactic uptake amplification*

$$R_U(t) = \frac{U_M(t) + U_{NM}(t)}{2U_{NM}(t)}. \quad (7)$$

The chemotactic uptake advantage, ΔU , quantifies the increase in the nutrient uptake rate due to chemotaxis. This is useful for analyzing the benefits of chemotaxis. However, for low nutrient concentrations, ΔU can be small even when motile bacteria consume the majority of available nutrients. In these cases, R_U gives a complementary metric for the enhancement of nutrient uptake by chemotactic bacteria relative to their non-motile counterparts.

Constraints on the potential benefit of chemotaxis can be described by three timescales. The chemotaxis timescale, $\tau_C = F_N \eta_N / V_C$, is the time needed for bacteria to reach the centre of nutrient filaments. The mixing timescale, $\tau_M = F_N^2 \eta_N^2 / \kappa_N = F_N^2 (\nu / \varepsilon)^{1/2}$, characterizes the time it takes for the filament of size $F_N \eta_N$ to fade away through diffusion once it reached the quasi-stationary state. Note that the impact of the diffusivity only appears in the Corrsin coefficient. Finally, the

uptake timescale, τ_U , is the inverse of the uptake rate associated with non-motile bacteria. The chemotactic uptake advantage can be scaled by means of Frost numbers (Grunbaum, 2002). The Frost numbers quantify the availability to consumers of spatially and temporally varying resource concentrations. In the case of turbulent mixing, two Frost numbers associated with mixing $\mathcal{F}r_M = \tau_C / \tau_M$ and uptake $\mathcal{F}r_U = \tau_C / \tau_U$ allow for a first-order scaling law of the time-integrated chemotactic uptake advantage (Taylor and Stocker, 2012),

$$\langle \Delta U \rangle = \int_0^\infty \Delta U dt \sim (2\mathcal{F}r_U + \mathcal{F}r_M)^{-1} \bar{N}^2 \Big|_{t=0}. \quad (8)$$

When $\mathcal{F}r_M > \mathcal{F}r_U$, mixing is faster than uptake, and the chemotactic uptake advantage is limited by mixing. On the contrary, when $\mathcal{F}r_U > \mathcal{F}r_M$, the chemotactic uptake advantage is limited by uptake.

4. Variability of the uptake rate

As discussed in the introduction, the uptake of dissolved nutrients by bacteria is an important element in many biogeochemical systems. In this paper, our primary objective is to assess how varies the effectiveness of chemotaxis in turbulent flows with respect to the environmental factors setting this biophysical interaction. Here, we focus on the influence of the dissipation rate ε , related to the level of turbulence, the chemotactic efficiency Γ , the swimming speed V_S and the chemotactic saturation length l_S , related to the motility of chemotactic bacteria, and finally the nutrient Schmidt number Sc_N , the patch half-width σ , and the uptake timescale τ_U , which are related to the nutrients behaviour and consumption. Tables C1 and C2 list the range of values considered. A full exploration of the parameter space using DNS would require a computational cost and time beyond the current resource limitations. Hence, the strategy used here is to vary only one environmental condition at a time around values used for the baseline simulation. This gives a measure of the influence of each parameter on the chemotactic uptake advantage.

We conduct a systematic analysis by studying in time a non-dimensional version of the instantaneous chemotactic uptake advantage

$$\Delta \tilde{U}(\tilde{t}) = \frac{\tau_U}{N_0} \Delta U(\tilde{t}) \quad \text{with} \quad \tilde{t} = \frac{t}{\tau_U}, \quad (9)$$

along with the chemotactic uptake amplification $R_U(\tilde{t})$, and the time-integrated uptake advantage

$$\langle \Delta \tilde{U} \rangle = \int_0^\infty \Delta \tilde{U} d\tilde{t}. \quad (10)$$

Below, we will use these definitions to quantify the absolute and relative uptake advantage conferred by chemotaxis.

4.1. Influence of the intensity of turbulence

As described earlier, varying the turbulent dissipation rate, ε , influences the length- and time-scales associated with the flow and scalar fields. With a high level of turbulence, $\varepsilon = 1.7 \times 10^{-6} \text{ m}^2 \text{ s}^{-3}$, stirring is strong and large nutrient gradients quickly develop. Chemotactic bacteria respond to these gradients and get a high maximum instantaneous uptake advantage $\Delta \tilde{U}$ (Fig. 3a). However, the mixing time τ_M is small, and before a third of the uptake timescale is reached ($\tilde{t} = 0.3$), nutrient gradients have disappeared, cancelling the chemotactic advantage. In this case, the bacterial uptake advantage is more limited by mixing ($\mathcal{F}r_M = 0.42$) than by uptake ($\mathcal{F}r_U = 0.04$). Chemotactic bacteria do not have time to create a strong advantage relative to the non-motile bacteria before the nutrient field is mixed, and chemotaxis only amplifies the instantaneous uptake by a maximum of 15% (see Fig. 3b).

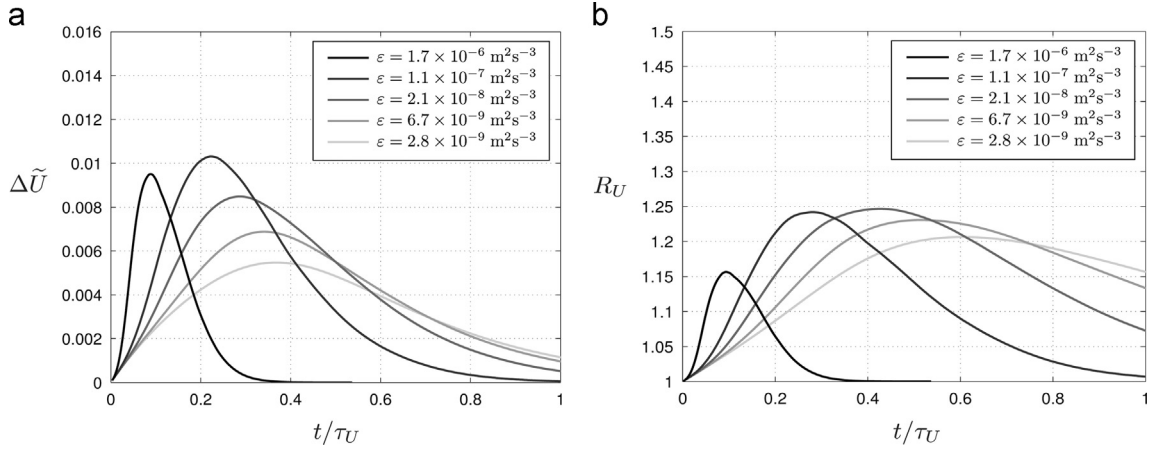


Fig. 3. Time evolution of the uptake advantage $\Delta\tilde{U}$ and amplification R_U for various values of the turbulent dissipation rates ε . Time is normalized by the uptake timescale τ_U . At large level of turbulence, the uptake advantage gets large but is quickly limited by mixing while at low level of turbulence the uptake advantage is low but lasts longer.

At the other extreme, for a low level of turbulence $\varepsilon = 2.8 \times 10^{-9} \text{ m}^2 \text{ s}^{-3}$, the nutrient filament lengthscale λ_N is larger, nutrient gradients are weaker and slower to develop, and the resulting instantaneous advantage $\Delta\tilde{U}$ is low and reaches its maximum later ($\tilde{t} = 0.4$). In this case, the bacterial uptake advantage is more limited by uptake ($\mathcal{F}r_M = 0.09$) than by mixing ($\mathcal{F}r_U = 0.19$).

The curves with intermediate values of dissipation rate ($\varepsilon = 1.1 \times 10^{-8}$, 2.1×10^{-8} and $6.7 \times 10^{-9} \text{ m}^2 \text{ s}^{-3}$) highlight the optimal trade-off where the level of turbulence is high enough to quickly create sharp nutrient gradients in order to induce high motility advantage, and the mixing is weak enough to give time for the motile bacteria to cluster around the filaments before gradients fade away (Taylor and Stocker, 2012). In these cases, the instantaneous uptake is amplified by up to 25% ($R_U = 1.25$).

The time difference between the maximum instantaneous uptake advantage $\Delta\tilde{U}$ and the maximum instantaneous uptake amplification R_U highlights the time lag associated with chemotaxis. With decreasing ε , the lifetime of nutrient gradients is larger (larger τ_M). Hence, although $\Delta\tilde{U}$ decreases after some time because a large fraction of nutrients has been already consumed, nutrient gradients are still present and motile bacteria continue to aggregate in the areas of larger nutrient concentration. The ratio of motile to non-motile bacteria concentration continues to increase, and chemotactic bacteria continue to amplify the uptake rate i.e. R_U continues to increase. Thus, a large difference between the time of maximum $\Delta\tilde{U}$ and the time of maximum R_U indicates that a non-negligible number of bacteria arrive at the core of nutrient filaments after the time window of large uptake advantage.

Fig. 4 shows the time-integrated uptake advantage $\langle \Delta\tilde{U} \rangle$. The maximum chemotactic uptake advantage lies between $\varepsilon = 2.1 \times 10^{-8}$ and $\varepsilon = 1.1 \times 10^{-8} \text{ m}^2 \text{ s}^{-3}$, which is consistent with earlier work (Taylor and Stocker, 2012). Note, however, that this optimal dissipation rate is found by holding the Reynolds number Re_λ fixed for all simulations, which therefore fixes the Corrsin coefficient, F_N (see Eq. (A.5)). An analysis of Eq. (8) shows that the chemotactic advantage is maximum, with respect to variations of $F_N \eta_N$, when $2\mathcal{F}r_U = \mathcal{F}r_M$. Therefore, we anticipate that varying Re_λ will influence F_N and therefore λ_N , and thereby influence the optimal dissipation rate. The impact of the Taylor Reynolds number on the optimal dissipation rate is discussed further in Section 5.

4.2. Influence of the motility of chemotactic bacteria

The motility of chemotactic bacteria, with a run and tumble motility pattern, is characterized by the speed of their runs, V_S , their chemotactic efficiency Γ , i.e. the ability of bacteria to

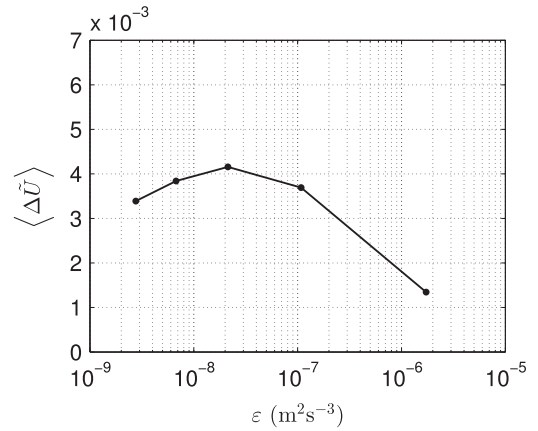


Fig. 4. Time-averaged uptake advantage $\langle \Delta\tilde{U} \rangle$ with respect to the turbulent dissipation rate ε . An optimized value emerges highlighting the trade-off between a strong chemotactic response to the sharp nutrient gradients created by a large level of turbulence and a long nutrient gradients lifetime resulting from a low level of turbulence.

introduce a bias in their random walk to swim predominantly toward positive nutrient gradients, and by their chemotactic saturation length l_S , i.e. the sensitivity of bacteria to nutrient gradients. The nutrient conservation equation (1a) can be non-dimensionalised by the initial peak concentration N_0 . Although it does not appear directly in the non-dimensional equation, N_0 influences Γ , as explained in Appendix B. To simplify the analysis, N_0 is kept constant here, while Γ is varied. The range of values of V_S studied here is broad ($68 - 347 \mu\text{m s}^{-1}$), and reflects the high variability of bacteria properties (Johansen et al., 2002; Barbara and Mitchell, 2003; Seymour et al., 2009). For simplification, the tumbling timescale is kept constant $\tau_S = 1\text{ s}$, and the persistence angle α is taken to be zero. The chemotactic saturation length, l_S , varies in a range of values already studied in experiments conducted in previous works (Ahmed and Stocker, 2008a; Stocker et al., 2008).

Fig. 5a shows the evolutions in time of the chemotactic advantage $\Delta\tilde{U}$, and amplification R_U for Γ , V_S and l_S , and Fig. 6a–c shows their corresponding time-integrated uptake advantage $\langle \Delta\tilde{U} \rangle$. An increase of any of these factors induces an improved ability of the chemotactic bacteria to reach rich-nutrient spots, and evidently leads to enhanced uptake of nutrients. A more surprising general result is that while characteristics of the motility of chemotactic bacteria clearly affects the uptake advantage, it does not modify much the timescale of maximum uptake advantage and

amplification. However, while no shift of the time maximum can be seen when varying l_S (Fig. 5a and b in blue), a slight shift to earlier times occurs for both Γ and V_S (Fig. 5a and b in green and red).

Decreasing Γ while keeping V_S fixed decreases V_C and hence increases the chemotaxis timescale, τ_C . Since all other parameters are held constant, decreasing Γ therefore decreases both $\mathcal{F}r_U$ and $\mathcal{F}r_M$, and eventually causes either mixing or uptake to limit the effectiveness of chemotaxis and decreases the uptake advantage (see (8)). The time-integrated uptake rate increases almost linearly for small values of Γ (Fig. 6a), consistent with a previous theoretical prediction (Taylor and Stocker, 2012) which is valid when fluctuations in the motile bacteria field are small. However, at larger Γ , $\langle \Delta \tilde{U} \rangle$ does not increase as rapidly, showing that the chemotactic uptake advantage exhibits limiting behaviour. This

can be understood by considering a limiting case with infinitely fast chemotaxis. Suppose that chemotaxis was fast and effective enough to ensure that all motile bacteria sampled the maximum concentration of nutrients at every instant in time. This hypothetical situation of “perfect co-localization” would optimize the chemotactic advantage, $\langle \Delta \tilde{U} \rangle$, at a finite value. Larger values of Γ would therefore be unable to increase the uptake advantage which should eventually reach a limiting value.

The case of perfect co-localization also applies to the swimming speed, hence the non-linear increase of $\langle \Delta \tilde{U} \rangle$ at large values of V_S (the solid line in Fig. 6b). However, varying V_S changes the chemotactic speed V_C but also the diffusivity coefficient κ_B . At late times, the curves $\Delta \tilde{U}$ and R_U collapse for all V_S . This contrasts with results obtained when varying Γ , where curves remain distinct (Fig. 5a in green and red). The collapse of the uptake curves at late

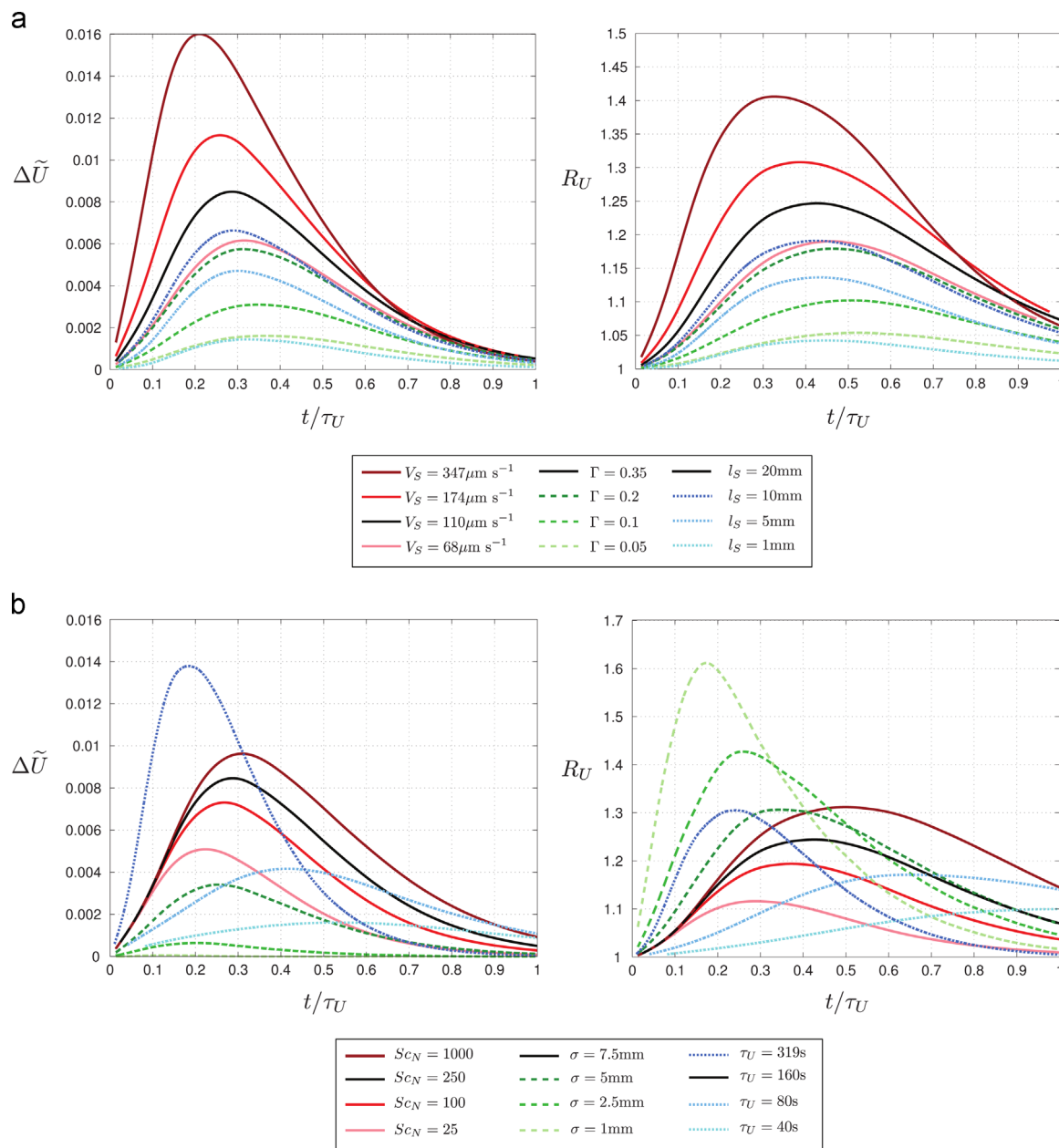


Fig. 5. Time evolution of the uptake advantage $\Delta \tilde{U}$ and amplification R_U for various values of (a) the chemotactic efficiency Γ , swimming speed V_S and chemotactic saturation length l_S and (b) the nutrient Schmidt number Sc_N , initial nutrient patch size σ and uptake timescale τ_U . The black curves represent the baseline simulation, around which each parameter is varied. Time is normalized by τ_U . (a) Motility related parameters. (b) Nutrient related parameters. (For interpretation of the references to color in this figure, the reader is referred to the web version of this paper.)

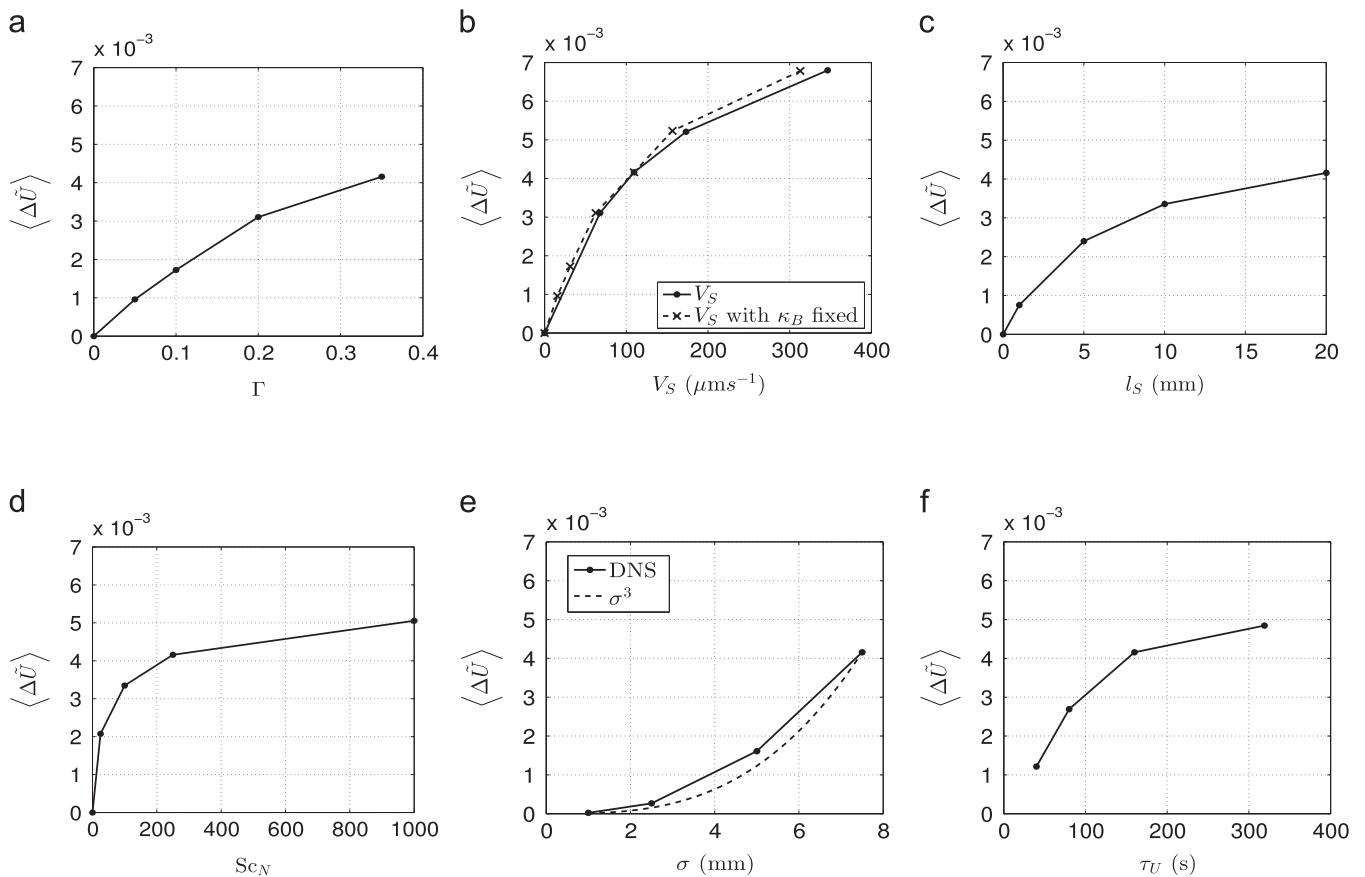


Fig. 6. Time-averaged uptake advantage $\langle \Delta \bar{U} \rangle$ with respect to the chemotactic efficiency Γ , the swimming speed V_S , the chemotactic saturation length l_S , the nutrient Schmidt number Sc_N , the nutrient patch size σ and the uptake timescale τ_U .

times can therefore be attributed to the influence of diffusion through random motility, κ_B . At late times, the width of bacteria filaments is set by a balance between the tendency for chemotaxis and stirring to sharpen the filaments of high bacteria concentration, and the action of diffusion to broaden the bacteria filaments. Increasing V_S in our simulations enhances chemotaxis and diffusion, and these two effects eventually cancel to some degree during the later stages of the process. For the range of swimming speeds studied here, the strategy of chemotaxis grants to motile bacteria a large advantage over non-motile bacteria, and motility amplifies the instantaneous uptake rate by at least 20% up to 40% (Fig. 5b in red).

The dashed line in Fig. 6b shows the time-integrated uptake advantages when varying V_S but keeping κ_B fixed (equivalent to varying Γ in our model). This set of simulations can be interpreted as varying the motility timescale, τ_S such that it balances the change in V_S to keep κ_B fixed (Taylor and Stocker, 2012). At large swimming speed, the uptake advantage is higher if the diffusion is weaker, thus showing the gain of uptake motile bacteria obtain by reducing their run duration to keep their diffusion constant (Seymour et al., 2009; Taylor and Stocker, 2012). However, despite a non-negligible impact of diffusion on $\Delta \bar{U}$ at late times, the resulting variation of the time-integrated uptake advantage due to diffusion is weak.

Finally, the time-integrated uptake advantage increases with l_S but not indefinitely (Fig. 6c). The uptake advantage begins to saturate for large values of l_S . This could be due to the limiting case of perfect co-localization, as with Γ or V_S . However, another mechanism might be responsible for the reduced sensitivity at large values of l_S . When l_S becomes very large, even broad nutrient

filaments with weak gradients will elicit the maximum chemotactic response with velocity V_C . In this case, the chemotactic response curve ($V_C(\nabla C)$) becomes close to a step function, and further increases in l_S will not provide a further increase in the uptake advantage.

4.3. Influence of the nutrients behaviour and consumption

In our model, the behaviour and consumption of nutrients are characterized by the nutrient initial patch size σ , the nutrient Schmidt number Sc_N , and the uptake timescale τ_U . Due to numerical limitations, it is not possible to explore the full range of patch sizes σ . The small sizes characteristic of many phytoplankton cells (Jackson, 2012) would require a high grid resolution which corresponding DNS could not be conducted in reasonable time. However, the range of values explored here allows to draw a clear trend of the uptake rate with changing nutrient patches size. Since the kinematic viscosity, ν , is fixed in our simulations, varying $Sc_N = \nu/\kappa_N$ is equivalent to varying the nutrient diffusivity, κ_N . A nutrient Schmidt number of $Sc_N \geq 1000$ is typical of dissolved nutrients in aquatic ecosystems (Jackson, 2012). Although lower values of Sc_N are less realistic, again, they allow the establishment of a scaling of the uptake rate with Sc_N , and moreover facilitate here comparison with earlier work where a lower Sc_N was used (Taylor and Stocker, 2012).

As previously stated, both bacteria populations are assumed to have the same mean concentration $\bar{B}_M = \bar{B}_{NM} = B_0$. To simplify the sensitivity study, τ_U is varied independently from κ_N and Sc_N . Thus, since the bacterium's characteristic diameter a is kept constant for all simulations ($a = 1 \mu\text{m}$), varying τ_U with a constant κ_N , or

varying κ_N with fixed τ_U , implies that the bacteria concentration B_0 varies to compensate.

Fig. 5b shows the evolutions in time of the chemotactic advantage $\Delta\tilde{U}$, and amplification R_U for Sc_N , σ and τ_U , and Fig. 6d–f shows their corresponding time-integrated uptake advantage $\langle\Delta\tilde{U}\rangle$. The behaviour of the nutrients largely affects the uptake advantage and strongly impacts the timescale of the biophysical interaction.

Increasing Sc_N , and therefore decreasing κ_N , allows nutrient filaments to develop on smaller scales during the quasi-stationary state (smaller $\lambda_N^{QSS} = F_N\eta_N$). The mixing timescale, $\tau_M = F_N^2(\nu/\varepsilon)^{1/2}$, is weakly sensitive to diffusivity (through the Corrsin coefficient, it increases by only 15% for a fortyfold increase in Sc_N). However, as λ_N^{QSS} is smaller for large nutrient Schmidt numbers, the time to reach the quasi-stationary state is longer. Hence, at larger Sc_N , the combination of slightly longer mixing and a longer transient gives more time to the motile bacteria to reach rich-nutrient spots, resulting in a larger maximum instantaneous chemotactic advantage and amplification (Fig. 5b in red).

While the time associated with the maximum instantaneous $\Delta\tilde{U}$ does not vary much with respect to Sc_N , the time associated with the maximum R_U is affected. Indeed, at large Sc_N , the nutrient gradients are large and remain above the threshold gradient defined by l_s/N_0 for a longer time (not shown here). As a result, chemotaxis is effective for a longer time.

The sensitivity of $\Delta\tilde{U}$ on Sc_N is weak. A fortyfold decrease in Sc_N reduces the maximum uptake advantage by a factor of two. For $Sc_N = 1000$, a realistic value in the ocean (Jackson, 2012), chemotaxis amplifies the total instantaneous uptake rate by up to 30% relative to non-motile bacteria ($R_U=1.3$). Increasing Sc_N by a factor of four from 250 to 1000 increases $\langle\Delta\tilde{U}\rangle$ by only 20% (Fig. 6d). It is however important to note that the uptake timescale τ_U is kept constant. Varying κ_N in reality could simultaneously change τ_U and Sc_N .

When varying the initial size of the injected nutrient patches, we held the peak concentration, N_0 , fixed. As a result, the initial integrated nutrient concentration of the spherical patch $\overline{N}(t=0)$ varies with σ^3 , and this increase is largely responsible for the large increase in the uptake advantage (Fig. 6b in green). However, changing the patch size has other effects. A smaller patch width reduces the duration of the transient period, allowing the quasi-stationary state to be reached more quickly. At this scale, the combination of stirring and diffusion erases the fluctuations in the nutrient field, therefore reaching this regime faster effectively decreases the lifetime of nutrient gradients. As a result, motile bacteria have less time to create an advantage before the nutrient patch is mixed. On the other hand, the initial nutrient gradient varies with N_0/σ , and smaller initial patch sizes help motile bacteria quickly reach their maximum chemotactic speed V_c . This effect appears to cause a large chemotactic amplification at early times in the simulation with the smallest patch size. In this case, chemotaxis can amplify the instantaneous total uptake by more than 60% ($R_U=1.6$). However, the early amplification of the chemotactic response is countered by a reduced response at later times when the nutrient patch becomes mixed.

The time-integrated uptake advantage increases approximately as a function of σ^3 (Fig. 6e), indicating that $\langle\Delta\tilde{U}\rangle$ is, to leading order, proportional to $\overline{N}(t=0)$. Thus, overall, chemotactic bacteria create a larger advantage for larger patch size σ because the initial volume of nutrients is larger. This entails that the gain of uptake advantage due to large initial gradients is compensated by the loss of uptake due to a small patch lifetime.

Varying τ_U in our simulations changes the rate at which both motile and non-motile bacteria consume nutrients. Both the simulation time and the uptake advantage are normalized by τ_U in Fig. 5b, i.e. $\tilde{t} = t/\tau_U$ and $\Delta\tilde{U} = \Delta U/(N_0/\tau_U)$ respectively. Increasing

τ_U eases the limitation imposed by the uptake timescale. Indeed, for our parameters, when $\tau_U = 320$ s, $\mathcal{F}_M = 0.14$ and $\mathcal{F}_U = 0.06$, and we expect the chemotactic response to be more limited by mixing. On the other hand, when $\tau_U = 40$ s, $\mathcal{F}_M = 0.10$ and $\mathcal{F}_U = 0.71$, and we anticipate that uptake will become a more limiting factor. This interpretation is supported by the DNS (Fig. 5b in blue). A long uptake timescale ($\tau_U = 320$ s) allows the motile bacteria to generate a large advantage and amplification (up to 40% with $R_U=1.4$), and enhances the integrated uptake by nearly a factor of 5 compared with the simulation with $\tau_U = 40$ s (Fig. 6f). However, as τ_U becomes very large and the uptake advantage becomes more limited by mixing, the integrated uptake advantage becomes less sensitive to τ_U . Finally, decreasing τ_U greatly increases the timescale of maximum uptake advantage and amplification, therefore switching from mixing-limited to uptake-limited maximum timescale.

5. Discussion

In this paper, Direct Numerical Simulations (DNS) have been used to study the response of chemotactic bacteria to dissolved nutrients in a turbulent flow. In particular, we explored the sensitivity of the advantage conferred by chemotaxis to a variety of physical and biological conditions. The simulations were set up as a competition between motile and non-motile bacteria. Although the equations governing the flow, nutrient, and bacteria fields are idealized and employ a number of simplifying assumptions, there are still many physical and biological parameters that govern the response of chemotactic bacteria. Here, we built upon earlier work (Taylor and Stocker, 2012) by varying physical and biological parameters to cover a wider range of parameter space. At the start of each simulation, a patch (or series of patches) of dissolved chemoattractant was released into a fully developed, homogeneous, isotropic turbulent flow. Two populations of bacteria, one motile and chemotactic, the other non-motile, are uniformly distributed throughout the computational domain at the start of each simulation. The non-motile bacteria remain uniformly distributed at subsequent times, while the motile bacteria cluster within nutrient filaments through chemotaxis.

The sudden injection of small pulses of dissolved organic matter is a frequent occurrence in the ocean's water column (for an overview, see Stocker, 2012). A primary example is represented by the lysis of small photosynthetic organisms, such as diatoms, either due to stress or viral infection. These lysis events can occur over seconds to minutes and result in the injection of DOM into the surrounding fluid. A second example is represented by sloppy feeding events, whereby larger organisms incompletely inject prey, resulting in the spillage of DOM in the surrounding fluid. A third example is the excretions by larger organisms such as copepods, which partly occur in the form of solid fecal pellets and partly as dissolved DOM, suddenly injected in the surrounding fluid. Here, we represent the injection of DOM using an array of Gaussian nutrient patches of varying size. Although this configuration is idealized, it allows us to focus on the response of chemotactic bacteria to an isolated DOM source in a turbulent flow under conditions that are representative of an ocean setting.

The evolution of the nutrient patches and bacteria response can be decomposed in three steps (Fig. 1). First, a transient regime appears in which stirring by the flow field elongates the original nutrient patch and decreases its characteristic lengthscale. This allows chemotactic bacteria to reach regions with high nutrient concentration more quickly, thereby enhancing the uptake of chemotactic bacteria relative to their non-motile counterparts. Then, in a quasi-stationary state (QSS), nutrient filaments reach a statistical equilibrium where diffusion counteracts stirring, and the

averaged nutrient lengthscale stays statistically constant. In the final regime, diffusion across nutrient filaments mixes the nutrient field, thereby bringing the instantaneous chemotactic advantage to zero.

Fig. 5a and b summarizes the sensitivity of the time-integrated uptake advantage to six of the environmental conditions we studied. In every case (except for σ which will be discussed later), the uptake advantage increases rapidly for small values of the parameter, but the sensitivity of the uptake decreases for large values of the parameter. Earlier work (Taylor and Stocker, 2012) found that the uptake advantage can be limited by one of two timescales associated with mixing and uptake, and the limiting factor can control the sensitivity of the uptake advantage. For example, when the uptake timescale is large, the uptake advantage will be limited by mixing and will be relatively insensitive to changes in the uptake rate. Here, we find that this limiting behaviour extends to all environmental factors studied here.

The tendency for the uptake advantage to saturate for large values of Γ , V_S and l_S might also be a reflection of an inherent limit to the uptake amplification that can be gained through motility. Although the scaling law in (8) predicts a linear increase in uptake with chemotactic velocity, this cannot extend indefinitely. For a given nutrient concentration field and a fixed number of bacteria, the maximum possible instantaneous uptake rate would be achieved by always placing all bacteria at the location of maximum nutrient concentration. Since chemotaxis corresponds to a rearrangement of bacteria cells, the uptake rate cannot exceed this upper bound that we call the perfect co-localization. Moreover, this most optimized case depends on the nutrient distribution and will therefore depend on the physical and biological conditions influencing the distribution of nutrients, including ε , Sc_N , κ_B , σ , and ℓ_p . More uniform nutrient distributions will allow less distinction between motile and non-motile uptake rates and will result in a lower upper bound uptake advantage.

Two new results that are worth highlighting concern the sensitivity of the uptake advantage to the diffusivity associated with the nutrient and bacteria concentrations. The diffusivity of the nutrient field, κ_N , can be described in terms of the Schmidt number, $Sc_N = \nu/\kappa_N$. Due to computational constraints, the simulations previously conducted (Taylor and Stocker, 2012) considered values up to $Sc_N = 300$, although realistic values of Sc_N are higher. Here, we conducted a simulation with $Sc_N = 1000$, a value commonly found in aquatic ecosystems (Jackson, 2012). Interestingly, the uptake advantage in this case is not significantly larger than the baseline case with $Sc_N = 250$, even though the uptake advantage is highly sensitive to the diffusivity at lower values of Sc_N . The factors behind the reduced sensitivity to Sc_N at high values are not fully understood. However, note that the diffusivity associated with motile bacteria is held fixed in the simulations with varying Sc_N , and the corresponding Schmidt number for motile bacteria is $Sc_B = \nu/\kappa_B = 250$. One possibility is therefore that diffusion of the motile bacteria prevents them from accumulating inside the thin nutrient filaments associated with large Sc_N . Another possible effect is that at such large Schmidt number, weak diffusion prevents the nutrient gradients from diffusing out to neighbouring chemotactic bacteria, thereby benefiting a smaller number of motile bacteria. This could enhance the disparity between the chemotactic benefit to motile cells, although the average motile uptake may not be strongly affected. A local analysis of the interaction between motile bacteria and the filament could provide further insight.

A second interesting result concerns the influence of the bacterial diffusivity κ_B . Varying the swimming speed V_S and holding the timescale τ_S fixed in Eq. (3) implies that the diffusivity κ_B will also vary. On the other hand, varying the chemotactic speed V_C (or Γ) with fixed V_S and τ_S will not influence κ_B . In the baseline study,

nutrient and bacterial diffusivities are equal. Our results show that the uptake advantage is slightly larger when bacteria diffuse at the same rate as nutrients (varying V_S and τ_S to keep $\kappa_B = \kappa_N$) than when bacteria diffuse less than nutrients (Fig. 6b). Although the difference in uptake advantage between the two cases is negligible, it remains unexpected that the uptake advantage is lower when $\kappa_B < \kappa_N$ than when $\kappa_B = \kappa_N$ for the same V_S since one might expect a larger uptake advantage in the case with smaller κ_B since with weaker diffusion, motile bacteria can accumulate more tightly near the locations of maximum nutrient concentration.

The maximum uptake advantage at $\kappa_B = \kappa_N$ could possibly highlight the trade-off for chemotactic bacteria between the search for nutrients by scanning an area as large as possible (when large κ_B is an advantage) and, once the nutrient gradients have been detected, swim and stay in regions of large nutrient concentration (when small κ_B is an advantage). By matching nutrient diffusion, motile bacteria optimize their chance to find high nutrient concentration regions and remain there. Moreover, the uptake advantage is insensitive to features in the bacteria field which are much smaller than the nutrient field (see Appendix A.4). A possible explanation is that once bacteria cluster tightly at the core of the nutrient filaments, the nutrient field is relatively constant on the smaller scale of the bacteria filament. At that point, clustering more tightly (as would occur with $\kappa_B < \kappa_N$) does not lead to an increase in the uptake advantage. Note that, due to the chemotactic term, the equality $\kappa_B = \kappa_N$ does not imply that the nutrient and bacteria filaments have equal lengthscales. In our simulations, κ_B had a significantly smaller influence on the uptake advantage compared to V_S , when varied about the baseline simulation. It is possible, however, that the results will be more sensitive to κ_B for larger values of the nutrient Schmidt number, Sc_N . When Sc_N is large, nutrient filaments are very thin, and the distribution of motile cells may be more sensitive to the influence of diffusion.

The instantaneous chemotactic amplification is very high for small patch sizes (Fig. 5b). Due to computational restrictions, the smallest initial nutrient patch size, σ , considered here was 1 mm. We expect chemotaxis to further amplify the nutrient uptake for patch sizes between 1 mm and the Batchelor scale ($\sim 200 \mu\text{m}$ in the ocean Jackson, 2012). Phytoplankton are an important source of chemoattractants in aquatic systems (through leakage or lysis), and many are much smaller than the Batchelor scale (Jackson, 2012). When chemoattractants are released at scales smaller than the Batchelor scale, diffusion is expected to dominate the early stages of these patches before they reach the Batchelor scale. In this case, simple flow models such as the one used by Locsei and Pedley (2009) might be appropriate to describe the early stages of the chemotactic response.

When varying the turbulent dissipation rate, ε , and holding other parameters fixed, we found that the uptake advantage is optimal for an intermediate level of turbulence, $\varepsilon \simeq 10^{-8} - 10^{-7} \text{ m}^2 \text{ s}^{-3}$. This finding is in agreement with results of Taylor and Stocker (2012) who explained the optimal turbulence level as a balance between the competing effects of stirring and mixing. From Eq. (8), we can infer that the maximum chemotactic advantage occurs when the uptake Frost number is equal to the mixing Frost number $2Fr_U = Fr_M$ (the factor 2 is because there are two populations). Hence, the optimal chemotactic advantage would occur when the uptake timescale $\tau_U/2$ is equal to the mixing timescale τ_M . The corresponding optimal dissipation rate is

$$\varepsilon_{\text{opt}} = F_N^4 \frac{4\nu}{\tau_U^2} \quad (11)$$

where F_N is the Corrsin coefficient defined in Eq. (A.5).

One of the simplifying assumptions that we made in our numerical simulations was that the Taylor Reynolds number of the

flow, Re_λ , is fixed for all simulations. This allowed us to fix the scale separation between the Kolmogorov scale and the domain size and hence ensure that none of the simulations become fully laminar at the flow scales. One important consequence of this assumption is that the Corrsin coefficient is constant across the simulations which implies that the nutrient filament does not depend on the Taylor Reynolds number Re_λ . However, Eqs. (11) and (A.5) suggest the opposite. Fig. 7 shows the scaling for the uptake advantage from Eq. (8) as a function of the dissipation rate ε and the Taylor Reynolds number. The magenta curve shows the optimal dissipation rate ε_{opt} for a given Re_λ . The optimal dissipation rate varies considerably with the Taylor Reynolds number. Directly testing this prediction at large Reynolds number would require extremely large and costly simulations, which are beyond our capacity at this time.

The optimal dissipation rate corresponds to a predicted maximum in the uptake advantage for a (fixed Taylor Reynolds number. However, in realistic flows with varying turbulence levels, we anticipate that the dissipation rate and the Taylor Reynolds number will not be independent, but will both vary as the turbulence changes. For instance, in a turbulent shear layer in a state of production/dissipation balance, the Taylor Reynolds number depend on the dissipation rate and the local shear $Re_\lambda \sim (\varepsilon/S^2)^{1/2}$ (Corrsin, 1958; Smyth, 2000). In stratified fluids like the ocean, the dissipation rate, ε , will also be influenced by the local shear and density stratification (MacKinnon and Gregg, 2003). However, details of the dependence between the dissipation rate, Taylor Reynolds number, levels of shear and stratification is still the subject of active research in the oceanography and turbulence communities. Since large Taylor Reynolds numbers are very difficult to obtain in numerical simulations, particularly with weakly diffusive tracers as is the case here, laboratory experiments might be useful to test the scaling law for how the uptake advantage scales with ε and Re_λ when both are allowed to vary.

Another simplifying assumption in our application of the Keller–Segel model was that the swimming speed, V_S , is constant in time and equal for all cells. There is evidence that bacterial swimming speed is adaptive, combining intermediate cruising speeds for exploration with fast hunting speeds upon encounter of a patch (Seymour et al., 2009). The ability of individuals to modulate their swimming speed in response to local nutrient conditions could further favour motile cells by enhancing chemotaxis when needed without expending unnecessary energy. We have also assumed that the efficiency of chemotaxis is constant. Locsei and Pedley (2009) found that the chemotaxis of *E. coli* in a linear shear flow becomes ineffective when the shear rate is higher than 2 s^{-1} . Rusconi et al. (1914) recently validated this result using experiments in a microfluidic device. The rate of strain in the

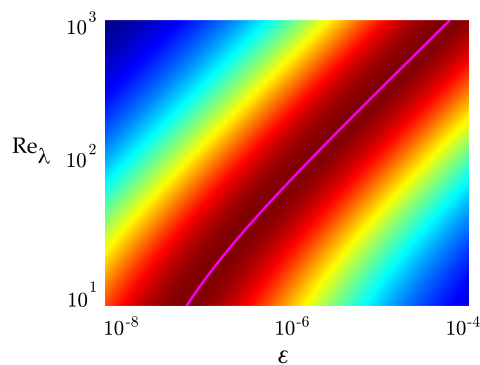


Fig. 7. Uptake advantage using the scaling law $(2\mathcal{F}r_U + \mathcal{F}r_M)^{-1}$ from Eq. (8) with values of the baseline simulation. The curve in magenta represents the maximum uptake advantage when $\varepsilon_{opt} = F_N^A \nu / (\tau_U/2)^2$. (For interpretation of the references to color in this figure caption, the reader is referred to the web version of this paper.)

strongest turbulence considered here (with $\varepsilon = 10^{-6} \text{ m}^2 \text{ s}^{-3}$) is $(\varepsilon/\nu)^{1/2} = 1 \text{ s}^{-1}$, suggesting that shear might affect chemotaxis, but probably would not eliminate its effectiveness. However, as turbulence is highly intermittent, the local shear can be up to two orders of magnitudes larger than its root mean square value (La Porta et al., 2001; Biferale et al., 2004; Seuront, 2008). It would be relevant to assess how much these local shear barriers affect the chemotactic advantage.

The fundamental reason for assuming diffusion-limited uptake in our model is the fact that nutrient concentrations in the ocean are typically low (Williams, 2000), and thus the linear uptake regime frequently applies. It is possible that in the core of filaments concentrations of DOM are high enough to saturate uptake. This case is not included in our model, and results in a potential overestimate of the uptake rate in filaments. A future extension of the model could account for the transition between diffusion-limited and intracell-transport-limited uptake, which in turn calls for additional experimental evidence for the concentration at which this transition occurs for bacteria in the ocean.

Finally, we expect the specific form of the chemotactic speed (Eq. (4)) to weakly influence general results presented here. Except for the smallest value of chemotactic saturation length l_S , nutrient gradients developed by the turbulent mixing are always high enough so that the local chemotactic velocity saturates to its maximum value V_C at early times of the biophysical interaction (not shown here). Hence the specific form of chemotaxis is most important in the late stages of the mixing when nutrient gradients are low. However, here we have studied only one type of chemotactic behaviour seen in marine environments. The question of optimality in bacterial chemotaxis is one of the most intriguing aspects of microbial biophysics. Even in the case of quiescent environments, this question has not been fully answered. The issue is complex because chemotactic strategies depend on both (i) the swimming strategies (some bacteria reverse, others tumble, and this in turn depends on flagellation), and (ii) the sensing strategy. This complexity is compounded in a turbulent flow. We can speculate that marine bacteria may have evolved specific chemotactic strategies in response to their filamentous resource landscape, but a quantitative analysis would require a very substantial body of work that tests the performance of different strategies, and would possibly require the use of an individual based model for bacteria, rather than a continuum based model as used here.

6. Conclusion

We found that the nutrient uptake rate by chemotactic bacteria is sensitive to range of physical and biological factors. Chemotaxis can enhance the total instantaneous nutrient uptake rate by up to range 60% and allow chemotactic bacteria to absorb nutrients 2.2 times faster than non-motile. The thin nutrient filaments introduce a trade-off in the diffusivity associated with the random walk of motile cells. Large values of this diffusivity, κ_B , allows motile bacteria to leave regions devoid of nutrients and enhances the chemotactic advantage once the cells encounter nutrient gradients. On the other hand if $\kappa_B \gg \kappa_N$, motile cells will be unable to remain close to the nutrient-rich center of the filaments. We find that chemotaxis provides the maximum benefit when $\kappa_B = \kappa_N$. While the bacterial diffusivity weakly influences the uptake advantage in our simulations, this influence may be higher in the environment. Finally, we raise the issue that an optimized turbulent dissipation rate for the chemotactic advantage may not occur in the ocean as the Taylor Reynolds number varies with the turbulent dissipation rate. A set of controlled experiments could help address these open questions. Although perhaps more limited in

parameter space, DNS provides a powerful complimentary tool to couple fluid physics with microbial ecology. the may be higher

To conclude, this paper highlights the role of the different biological and physical parameters on the outcome of the competition. As such, our hope is that this work can guide others in considering microbial competition under realistic environmental conditions, by identifying the role and importance of the key parameters.

Acknowledgements

RW ran and analyzed the numerical simulations, R.W., R.S., and J.R.T. wrote the paper. R.W. was funded by the Isaac Newton Trust the University of Cambridge EPSRC Strategic Fund, and the Flagship Project RITMARE - The Italian Research for the Sea. R.S. gratefully acknowledges support from the Gordon and Betty Moore Foundation through a Marine Microbial Ecology Investigator Award (GBMF3783).The funding sources had no involvement in the making of the present work. The authors thank Tanvir Ahmed for sharing experimental data used in Appendix B.

Appendix A. Details on the methodology

A.1. Fluid flow governing equations

The turbulent velocity field is obtained by solving the incompressible Navier–Stokes equation for a fluid of constant density ρ_0 (equations given in their dimensional form)

$$\frac{\partial \mathbf{u}}{\partial t} + \mathbf{u} \cdot \nabla \mathbf{u} = -\nabla p + \mathbf{F} + \nu \nabla^2 \mathbf{u}, \tag{A.1a}$$

$$\nabla \cdot \mathbf{u} = 0, \tag{A.1b}$$

where \mathbf{u} is the fluid velocity, p is the pressure (here normalized by the density ρ_0), and ν is the fluid kinematic viscosity. A three-dimensional, statistically steady, homogeneous, isotropic turbulent flow is generated through the forcing term \mathbf{F} , which appears on the right hand side of the momentum equations. The forcing term, \mathbf{F} , is designed to generate a statistically steady target turbulent kinetic energy dissipation rate ε_T . In particular, each component of the forcing vector, F_α , is proportional to a low-pass filtered velocity \tilde{u}_α

$$F_\alpha = \frac{\tilde{u}_\alpha \varepsilon_T}{3 \tilde{u}_\alpha u_\alpha}, \tag{A.2}$$

where $\tilde{\cdot}$ is the average over the numerical domain, and \tilde{u}_α is the velocity field filtered at large wavenumber $|\mathbf{k}| > 2.5(2\pi/L)$, where L is the domain size. A similar method was used in Carati et al. (1995). The denominator ensures that no component will become much larger than the others. At steady state, the energy dissipation rate, $\varepsilon = -\nu \overline{\mathbf{u} \cdot \nabla^2 \mathbf{u}}$ is balanced by the rate of injected energy $\overline{\mathbf{F} \cdot \mathbf{u}}$, giving a fixed dissipation rate $\varepsilon = \varepsilon_T$. This approach is slightly modified from the method used in Taylor and Stocker (2012) where the dissipation rate was kept constant by amplifying the existing large-scale velocity. The method employed here has the advantage of maintaining a higher degree of flow isotropy.

A.2. Theoretical lengthscales and nondimensional numbers associated to the biophysical interaction

In the three-dimensional, homogeneous, isotropic turbulent flow considered here, the most energetic turbulent eddies have a characteristic integral lengthscale, $\lambda_I \equiv k^3/2\varepsilon$, where $k = \frac{1}{2}\overline{\mathbf{u}^2}$ is the turbulent kinetic energy. Here, we force the turbulence at large

scales and the integral lengthscale is close to the domain size, $\lambda_I \simeq L$. Then, through non-linearities of the flow, kinetic energy is transferred from large to small eddies, eventually reaching the Kolmogorov scale, $\eta_K \equiv (\nu^3/\varepsilon)^{1/4}$ (Kolmogorov, 1958), where viscous forces dissipate kinetic energy. The intensity of turbulence is often characterized using the Taylor Reynolds number, $Re_\lambda \equiv \lambda_I/\lambda_T$, where the Taylor microscale is $\lambda_T \equiv C_\lambda(\nu k/\varepsilon)^{1/2}$, with $C_\lambda = (20/3)^{1/2}$ (Tennekes et al., 1972; Pope, 2000). While the Kolmogorov scale provides a measure for the smallest motions in a turbulent flow, the Taylor microscale separates large scales that are relatively unaffected by viscosity, and small scales where viscosity has a strong, direct effect. In experiments, the Taylor microscale Reynolds number Re_λ typically varies from 20, for weakly turbulent flows, up to several thousand for highly turbulent flows (Pope, 2000, Section 6.5.4).

The size a of the bacterium is generally three orders of magnitude smaller than the Kolmogorov scale, hence at the scale of bacterium the fluid flow is entirely laminar. As a result, the transport of nutrient due to advection relies on the bacterium's swimming speed and is negligible compare to diffusion of nutrients (Karp-Boss et al., 1996), therefore giving a small Peclet number $Pe_B = V_S a/\kappa_N \ll 1$.

When a heterogeneous passive scalar P is released in a turbulent flow, the dissipation of the fluctuations occurs at the Batchelor scale, $\eta_P \equiv (\nu \kappa_P^2/\varepsilon)^{1/2}$ (Batchelor, 1959), where κ_P is the diffusivity of P . The Batchelor scale, η_P , is related to the Kolmogorov scale η_K and the ratio between the flow and scalar diffusivities, i.e. the Schmidt number $Sc_P = \nu/\kappa_P$, such that $\eta_P \equiv \eta_K/Sc_P^{1/2}$ (Batchelor, 1959). However, analogously to the turbulent kinetic energy, very little scalar variance remains at the Batchelor scale. Instead, a characteristic lengthscale associated with fluctuations in the scalar P can be defined by

$$\lambda_P = \left(\frac{\overline{P'^2}}{\overline{\nabla P} \cdot \nabla P} \right)^{1/2}, \tag{A.3}$$

where $P' = P - \bar{P}$ is the fluctuating component of the scalar field, and \bar{P} denotes an average of P over the domain. Thus, analogously to the Taylor microscale, the lengthscale λ_P provides an estimate of the lengthscale below which the scalar diffusivity directly affects the scalar heterogeneities and starts to destroy the fluctuations. Corrsin showed that the proportionality coefficient, F_P , such that

$$\lambda_P \approx F_P \eta_P, \tag{A.4}$$

is a function of the Taylor microscale Reynolds number Re_λ and the nutrient Schmidt number Sc_P (Corrsin, 1964). In the case studied here of isotropic flow and large Schmidt numbers, the coefficient F_P is

$$F_P = \left[\frac{C_\lambda^{-1} Re_\lambda}{2 + Sc_P^{-1}} \left(3 + C_\lambda Re_\lambda^{-1} \ln Sc_P \right) \right]^{1/2}. \tag{A.5}$$

A.3. Numerical set-up

Eqs. (A.1) and (1) are solved with direct numerical simulations (DNS) using a pseudo-spectral method based on Fourier transforms with periodic boundary conditions in all three directions. Time stepping in the code uses a combination of the explicit third-order Runge–Kutta scheme and a semi-implicit Crank Nicolson scheme. Details of the numerical method are available in Taylor (2008).

The setup used here is similar to that in Taylor and Stocker (2012). In a cubic domain $\mathcal{D} = L^3$, after the flow is in a quasi-stationary state with a constant dissipation rate ε , a pulse of spherical gaussian nutrient patches, of characteristic half-width σ and equi-spaced by the distance ℓ_p , is injected.

The kinematic viscosity ν remains constant for all simulations, and therefore the Kolmogorov scale $\eta_K \equiv (\nu^3/\varepsilon)^{1/4}$ is determined by the dissipation rate ε . Hence, if the domain size L is held fixed, a DNS with low ε would have a large η_K , and the ratio of the domain size to the Kolmogorov scale, $r_f = L/\eta_K$, is small. In this case, the Taylor Reynolds number Re_λ is small, viscosity influences all scales of motion, and the flow does not become turbulent. To avoid this issue in a computational domain of limited size, when varying the target dissipation rate ε_T , it is useful to keep r_f constant, i.e. to scale the domain size such as $L \sim \varepsilon_T^{-1/4}$, and sufficiently large to maintain a turbulent flow. As a result, the Taylor Reynolds number Re_λ remains constant for all simulations. This is achieved by varying both domain size and dissipation rate following $L = nL_1$ and $\varepsilon_T = \varepsilon_1/n^4$, respectively. In order to keep the spacing between nutrient patches constant as the domain size increases, multiple nutrient patches are released in simulations with lower dissipation rates. Specifically, the number of patches in a given simulation is $(L/\ell_p)^3 = n^3$, all equally spaced within the computational volume (see Fig. 1 for the case $n=3$). Hence, L_1 and ε_1 represent the domain size and dissipation rate for the simulation at large level of turbulence when a single patch of nutrients is released at the centre of the computational domain. Note that a lattice of nutrient patches is consistent with the periodic boundary conditions used in all cases.

A.4. Resolution of the DNS

To cancel potential numerical artefacts, the 2/3 de-aliasing technique is applied to the nutrient and bacteria fields in the DNS (Orszag, 1971). In order to accurately resolve the passive scalar, a commonly used criterion is that the grid-spacing δx must be smaller than twice η_p , i.e. $\delta x \leq 2\eta_p$ (Yeung et al., 2004; Donzis et al., 2010). Here, two Batchelor scales can be defined, η_N for the nutrient field, $P=N$, and η_B for the motile bacteria field, $P=B_M$. Through chemotaxis, motile bacteria can develop smaller-scale features than would be found for a passive tracer with the same diffusivity. However, we show here that the field $B_M N$, used to compute the uptake advantage, can be accurately calculated on a grid satisfying the usual criteria $\delta x \leq 2\eta_N$.

Eqs. (A.1) and (1) are solved with direct numerical simulations (DNS) using a pseudo-spectral method based on Fourier transforms with periodic boundary conditions in all three directions. Applying Orszag's technique (Orszag, 1971) for a simulation with m^3 gridpoints in a cubic domain of size L , the code solves the equations in the spectral space with a range of wavenumbers of $2\pi[0-m/2]/L$ in the three directions (x, y, z), and zeroes each field after the wavenumber $2\pi m/3/L$ $2\pi[m/3-m/2]/L$ $2\pi(m/2)/L$. This prevents spurious aliasing into lower wavenumbers. Details of the numerical method are available in Taylor (2008) and Taylor and Stocker (2012).

The uptake rate is quantified using the encounter term between bacteria and nutrient fields, $B_{NM}N$ and $B_M N$. To get an accurate uptake rate, it is therefore important to resolve all the scales involved in these interactions. To quantify the quality of resolution, the following correlation function is used, for all wavenumber defined in the simulation:

$$C_{BN}(t, k) = \frac{\widehat{\sigma}_B(t, k) \widehat{\sigma}_N(t, k)}{\widehat{\sigma}_B(t, k) \widehat{\sigma}_N(t, k)}, \quad (\text{A.6})$$

where $\widehat{\sigma}_\phi = \widehat{\phi} \widehat{\phi}^*$ is the variance of ϕ at time t and wavenumber $k = \sqrt{k_x^2 + k_y^2 + k_z^2}$. Only the term $B_M N$ is studying as it is the one in which small scales effects appears due to chemotaxis. The closer to 1 the correlation function $C_{BN}(t, k)$ at time t and wavenumber k , the better B_M and N are correlated at this scale and will influence the uptake rate.

Fig. A1 shows the correlation coefficient $C_{BN}(t, k)$ for four numerical simulations with a increasing number of nodes $[256^3, 384^3, 512^3, 786^3]$. The simulation 786^3 in Fig. A1d is well resolved, thus giving the converged value of the uptake rate. One can see that the correlation is high at large scales and then decreases with large wavenumbers. Hence, with a resolved simulation, small scales do not contribute to the uptake rate. However, when decreasing the number of nodes, the correlation function keeps large values at small scales, especially when the uptake rate is maximum around $t/\tau_U = 0.2$, therefore adding numerical artefacts to the uptake rate. However, these numerical artefacts mostly appear in the region $2\pi[m/3-m/2]/L$, therefore applying the 2/3 de-aliasing technique (Orszag, 1971) on the non-linear term $B_M N$ is enough to get rid of the influence of numerics on the uptake advantage. Fig. A2 shows the corresponding uptake rates without and with the cutoff filter. With the cutoff, the uptake rate is converged with only 384^3 nodes.

Thus, unlike in Taylor and Stocker (2012), no filter function is applied on the bacteria field. Instead, the cutoff scale is also applied on non-linear terms.

Appendix B. Chemotactic velocity

A Keller–Segel type model is used for chemotaxis (see Section Appendix A.1). The term \mathbf{V}_C of Eq. (1b) represents the chemotactic velocity, i.e. the component of bacteria's velocity directed toward positive nutrient gradients. It is shown in this section that the simplified tanh term, already used in earlier work (Taylor and Stocker, 2012), can be derived from existing models.

Many equations have been developed to model the chemotactic velocity. Among them, the 1D-model of Rivero et al. (1989) turns to be a simple but efficient approach to compute chemotaxis in a DNS. Rivero's model has then been extended in two dimensions by Ford and Cummings (1992) and in three dimensions by Chen et al. (1998), which is written as follows:

$$|\mathbf{V}_C| = \Gamma_T V_S = \frac{2}{3} V_S \tanh\left(\frac{\chi_0}{2V_S} \frac{K_D}{(K_D + N)^2} |\nabla N|\right) \quad (\text{B.1})$$

where $\Gamma_T = \max(|\mathbf{V}_C|/V_S)$ is the theoretical chemotactic efficiency, and depends on the local environment i.e. the nutrient concentration N and gradient $|\nabla N|$, and the physiological parameters i.e. the chemotactic sensitivity coefficient, χ_0 , and the receptor/ligand dissociation constant K_D . Eq. (B.1) shows that for large $|\nabla N|$ or small N , bacteria increase their chemotactic velocity up to a theoretical maximal chemotactic speed $2/3V_S$ which is lower than V_S . This reflects the limitation due to the random walk strategy. However, experiments showed that, in an environment of large nutrient concentrations and gradients, the adaptation response of bacteria actually saturates at lower values than $2/3V_S$, and it takes seconds to minutes before bacteria adapt and increase again their chemotactic velocity (Berg and Tedesco, 1975; Block et al., 1982). At this stage, Rivero's model breaks down (Block et al., 1983; Ahmed and Stocker, 2008a). This can be corrected by using the bacteria critical adaptation ramp a_{crit} above which the regime is saturated

$$\text{if } \frac{|\nabla N|}{2N} V_S > a_{\text{crit}} \quad \text{then} \quad |\mathbf{V}_C| = \frac{2}{3} V_S \tanh\left(\frac{\chi_0 a_{\text{crit}}}{V_S} \frac{K_D N}{(K_D + N)^2}\right), \quad (\text{B.2})$$

The critical adaptation ramp is determined experimentally (Block et al., 1983). The saturated chemotactic efficiency Γ can then be modelled with the nutrient concentration and the critical ramp such as

$$\Gamma = \frac{2}{3} \tanh\left(\frac{\chi_0 a_{\text{crit}}}{V_S} \frac{K_D N}{(K_D + N)^2}\right). \quad (\text{B.3})$$

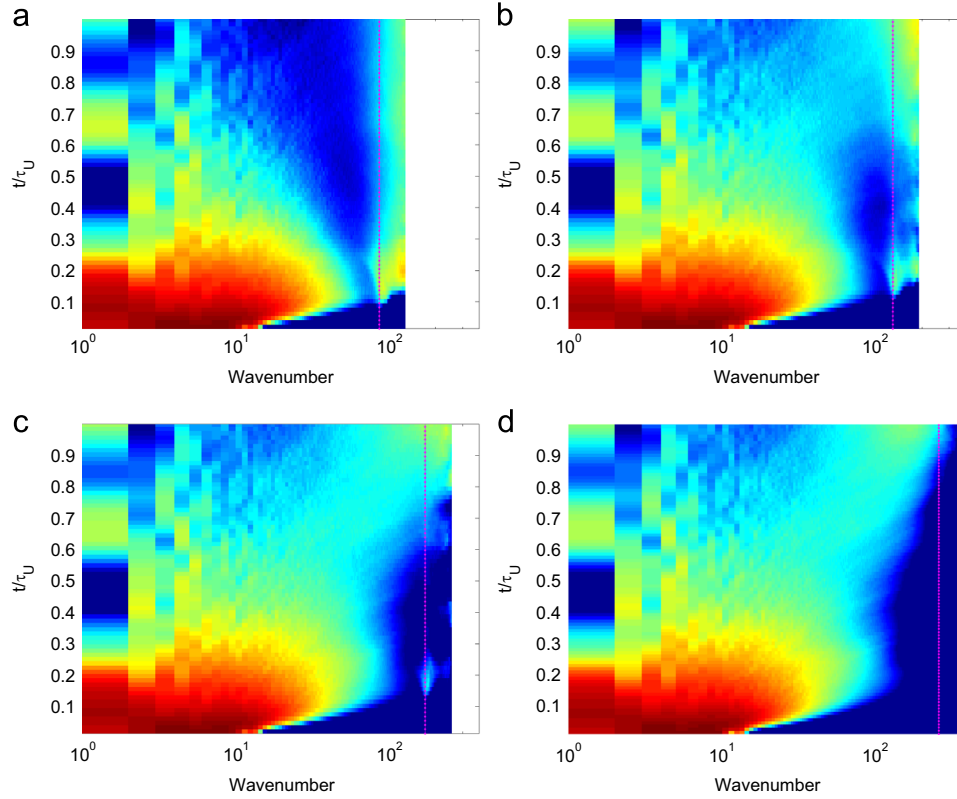


Fig. A1. Correlation function $C_{BN}(k, t)$ as a function of the mode numbers $[1, m]$ and time for various mesh size. The colorbar is held fixed in the range $C_{BN} = [0.5 - 1]$. Dotted magenta line represents the $2/3$ de-aliasing threshold after which the field is zeroed. The correlation drops at small scales, but due to numerical discrepancies, rises again. (a) 256^3 (b) 384^3 (c) 512^3 (d) 768^3 . (For interpretation of the references to color in this figure caption, the reader is referred to the web version of this paper.)

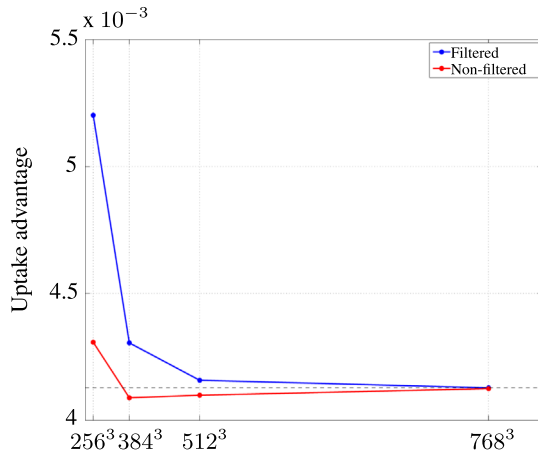


Fig. A2. Time-integrated uptake advantage $\langle \Delta \bar{U} \rangle$ as a function of the number of nodes m^3 . *Filtered*: a low-pass filter is applied to the motile field B_M to prevent numerical buildup in the variance (Taylor and Stocker, 2012). *Non-filtered*: no filter is used but the $2/3$ de-aliasing technique is applied to the non-linear term $B_M N$. Most of the uptake advantage is captured with a simulation with 384^3 nodes.

Thus, the chemotactic velocity is limited both by random walk, $\Gamma_T V_S$, and by saturation of the adaptation response ΓV_S

$$|\mathbf{V}_C| = \min(\Gamma_T, \Gamma) V_S. \quad (\text{B.4})$$

Since Γ is the limiting term, Eq. (B.4) is simplified in order to both have Rivero's model in its linear regime, i.e. when far from the saturation response, and the maximum chemotactic speed reachable,

$$V_C = \Gamma V_S$$

$$|\mathbf{V}_C| = V_C \tanh\left(\frac{2}{3} \frac{1}{\Gamma} \frac{\chi_0}{2V_S} \frac{K_D}{(K_D + N)^2} |\nabla N|\right). \quad (\text{B.5})$$

The chemotactic saturation length l_S of Eq. (4) (with $N = N_0$) can be therefore derived from Eq. (B.5)

$$l_S = \frac{1}{\Gamma} \frac{\chi_0}{3V_S} \frac{K_D N}{(K_D + N)^2}. \quad (\text{B.6})$$

Hence, one finds the logical results that chemotactic saturation length l_S and efficiency Γ are linked with the chemotactic sensitivity χ_0 . However Γ also depends on the critical ramp a_{crit} , thus combining Eqs. (B.3) and (B.6)

$$l_S = \frac{V_S}{2a_{\text{crit}}} \frac{\tilde{l}_S}{\tanh(\tilde{l}_S)} \quad \text{with} \quad \tilde{l}_S = \frac{\chi_0 a_{\text{crit}}}{V_S^2} \frac{K_D N}{(K_D + N)^2}. \quad (\text{B.7})$$

The chemotactic saturation length is a function of nutrient environment N and the physiology of bacteria ($V_S, a_{\text{crit}}, \chi_0, K_D$). However, the dissociation coefficient is usually larger than the nutrient concentration considered here $N \ll K_D$ (Mopper and Lindroth, 1982; Ahmed and Stocker, 2008a). As a result, $\tilde{l}_S / \tanh(\tilde{l}_S) \approx 1$ and one can approximate l_S such as

$$l_S \approx \frac{V_S}{2a_{\text{crit}}}. \quad (\text{B.8})$$

Ahmed and Stocker (2008a,b) determined experimentally the swimming speed, V_S , the chemotactic sensitivity, χ_0 , and the chemotactic efficiency as a function of the nutrient concentration and gradients $\Gamma(N, \nabla N)$ for E. Coli HCB1. Block et al. (1983) provided the critical ramp a_{crit} for the same strain. Results using (B.6) give a median experimental chemotactic saturation length of $l_S = 1.2$ mm with a minimum at l_S

= 0.27 mm and a maximum at $l_S = 3.5$ mm. Eq. (B.8) gives $l_S \approx 0.63$ mm $\tilde{l}_S/\tanh(\tilde{l}_S)$ varying from 1 to 1.25. Thus, Eq. (B.8) gives the good order of magnitude. It could be interesting to verify the scaling for other species.

Appendix C. Table of simulation parameters and scales

See Tables C1 and C2.

Table C1

Table of simulations parameters.

Symbol	Description	Baseline value	Value range	Units
Flow				
ν	Kinematic viscosity	10^{-6}		$\text{m}^2 \text{s}^{-1}$
ϵ_T	Turbulent dissipation rate	2.1×10^{-8}	2.8×10^{-9} – 1.8×10^{-6}	$\text{m}^2 \text{s}^{-3}$
Nutrient				
N_0	Initial concentration	25		μM
σ	Initial patch size	7.5	1–7.5	mm
κ_N	Nutrient diffusivity	4.0×10^{-9}	1.0×10^{-9} – 4.0×10^{-8}	$\text{M}^2 \text{s}^{-1}$
Sc_N	Nutrient Schmidt number	250	25–1000	
Bacteria				
a	Characteristic diameter	1.0		μm
τ_S	Mean run time	1.0		s
α	Persistence parameter	0.0		
B_0	Initial concentration	2.5×10^{11}	6.2×10^{10} – 1.0×10^{12}	cells m^{-3}
τ_U	Uptake timescale	160	40–320	s
Γ	Chemotactic efficiency	0.35	0.1–0.35	
V_S	Swimming velocity	114	68–346	μms^{-1}
l_S	Chemotactic saturation length	20	1–20	mm
Lengthscales				
η_K	Kolmogorov scale	2500	1000–4500	μm
$F_N \eta_N$	Nutrient lengthscale	700	200–1000	μm
λ_B	Bacteria lengthscale (from DNS)	250	70–330	μm
Simulations				
ϵ_p	Inter-patch distance	5.65		cm
n	Number of patches	3	1–5	
L	Computational domain size	17.0	5.65–28.25	cm
T	Flow timescale	9.0	1–25	s
N_g^3	Computational gridpoints	512 ³	384 ³ –1024 ³	
$Kn_M = V_C \tau_S / F_N \eta_N$	Knudsen number	0.06	0.01–0.07	

Table C2

Table of simulations nondimensional parameters.

Symbol	Description	Baseline value	Value range	
Flow				
$Re = L^2 / (T\nu)$	Flow Reynolds number	3200		
$Re_t = k^2 / (\epsilon\nu)$	Turbulent Reynolds number	95		
$Re_s = \lambda_t / \lambda_T$	Taylor Reynolds number	25		
Nutrient				
Sc_N	Nutrient Schmidt number	ν / κ_N	250	25–1000
Bacteria				
Pe_B	Bacteria Peclet number	$V_S a / \kappa_N$	3×10^{-2}	3×10^{-3} – 1×10^{-1}

References

- Ahmed, T., Stocker, R., 2008a. Experimental verification of the behavioral foundation of bacterial transport parameters using microfluidics. *Biophys. J.* 95, 4481–4493.
- Ahmed, Stocker, R., 2008b. Personal Communication.
- Al-Homoud, A., Hondzo, M.H., LaPara, T., 2007. Fluid dynamics impact on bacterial physiology: biochemical oxygen demand. *J. Environ. Eng.* 133, 226–236.
- Arin, L., Marrasé, C., Maar, M., Peters, F., Sala, M.-M., Alcatraz, M., 2002. Combined effects of nutrients and small-scale turbulence in a microcosm experiment. I. Dynamics and size distribution of osmotrophic plankton. *Aquatic Microbiol. Ecol.* 29, 51–61.

- Azam, F., Malfatti, F., 2007. Microbial structuring of marine ecosystems. *Nature* 5, 782–791.
- Baird, R.B., Smith, R.-K., 2002. Third Century of Biochemical Oxygen Demand. Water Environment Federation edn. Alexandria, Va.
- Barbara, G., Mitchell, J., 2003. Bacterial tracking of motile algae. *EMS Microb. Ecol.* 44 (1), 79–87.
- Batchelor, G.K., 1959. Small-scale variation of convected quantities like temperature in turbulent fluid. *J. Fluid Mech.* 5, 113–133.
- Beaton, R., 2007. A model for bacterial colonization of sinking aggregates. *Bull. Math. Biol.* 69 (1), 417–431.
- Berg, H.C., Tedesco, P.M., 1975. Transient response to chemotactic stimuli in *Escherichia coli*. *Proc. Natl. Acad. Sci. USA* 72, 3235–3239.
- Berg, H.C., 1983. *Random Walks in Biology*. Princeton University Press, Princeton, NJ.
- Bergstedt, M., Hondzo, M.H., Cotner, J.B., 2004. Effects of small scale fluid motion on bacterial growth and respiration. *Freshw. Biol.* 49, 28–40.
- Biddanda, B.A., Cotner, J.B., 2002. Love handles in aquatic ecosystems: the role of dissolved organic carbon drawdown, resuspended sediments, and terrigenous inputs in the carbon balance of Lake Michigan. *Ecosystems* 5, 431–445.
- Biferale, L., Boffetta, G., Celani, A., Devenish, B.J., Lanotte, A., Toschi, F., 2004. Multifractal statistics of Lagrangian velocity and acceleration in turbulence. *Phys. Rev. Lett.* 93 (6).
- Block, S.M., Segall, J.E., Berg, H.C., 1982. Impulse responses in bacterial chemotaxis. *Cell* 31, 215–226.
- Block, S.M., Segall, J.E., Berg, H.C., 1983. Adaptation kinetics in bacterial chemotaxis. *J. Bacteriol.* 154, 312–323.
- Brennen, C., Winet, H., 1977. Fluid mechanics of propulsion by cilia and flagella. *Annu. Rev. Fluid Mech.* 9, 339–398.
- Carati, D., Ghosal, S., Moin, P., 1995. On the representation of backscatter in dynamic localization models. *Phys. Fluids* 7 (606).
- Chen, K.C., Ford, R.M., Cummings, P.T., 1998. Perturbation expansion of Alt's cell balance equations reduces to Segel's one-dimensional equations for shallow chemoattractant gradients. *SIAM J. Appl. Math.* 59, 35–57.
- Clyne, J., Minni, P., Norton, A., Rast, M., 2007. Interactive desktop analysis of high resolution simulations: application to turbulent plume dynamics and current sheet formation. *New J. Phys.* 9 (301).
- Corrsin, S., 1958. Local Isotropy in Turbulent Shear Flow. N.A.C.A. RM58B11.
- Corrsin, S., 1964. The isotropic turbulent mixer II: arbitrary Schmidt number. *AIChE J.* 10 (870).
- del Giorgio, P.A., Duarte, C., 2002. Respiration in the open ocean. *Nature* 420, 279–384.
- Diaz, R.J., Rosenberg, R., 2008. Spreading dead zones and consequences for marine ecosystems. *Science* 321, 926–929.
- Donzis, A.D., Sreenivasan, K.R., Yeung, P.K., 2010. The batchelor spectrum for mixing of passive scalars in isotropic turbulence. *Flow Turbul. Combust.* 85, 549–566.
- Engelmann, 1883. *Bacterium photometricum*. *Pfl. ug. Arch. Gesamte Physiol.* 30, 95–124.
- Ford, R.M., Cummings, P.T., 1992. On the relationship between cell balance equations for chemotactic cell-populations. *SIAM J. Appl. Math.* 52, 1426–1441.
- Grunbaum, D., 2002. Prediction availability to consumers of spatially and temporally variable resources. *Hydrobiologia* 480, 175–191.
- Guasto, J.S., Rusconi, R., Stocker, R., 2012. Fluid mechanics of planktonic microorganisms. *Annu. Rev. Fluid Mech.* 44, 373–400.
- Hart, D.R., Stone, L., Berman, T., 2000. Seasonal dynamics of the Lake Kinneret food web: the importance of the microbial loop. *Limnol. Oceanogr.* 2 (45), 350–361.
- Jackson, G.A., 2012. Seascapes: the world of aquatic organisms as determined by their particulate natures. *J. Exp. Biol.* 215, 1017–1030.
- Johansen, J., Pinhassi, J., Blackburn, N., Zweifel, U., Hagstrom, A., 2002. Variability in motility characteristics among marine bacteria. *Aquatic Microbiol. Ecol.* 28 (3) 229–237.
- Karp-Boss, L., Boss, E., Jumars, P.A., 1996. Nutrient fluxes to planktonic osmotrophs in the presence of fluid motion. *Oceanogr. Marine Biol. Annu. Rev.* 34 (71), 71–107.
- Keller, E.F., Segel, L.A., 1970. A mathematical model for chemotaxis. *J. Theor. Biol.* 30, 225–234.
- Kjørboe, T., 2008. *A Mechanistic Approach to Plankton Ecology*. Princeton University Press, Princeton and Oxford, 2008.
- Kolmogorov, A.N., 1958. Dissipation of energy in a locally isotropic turbulence. *Am. Math. Soc. Transl.* 8 (2), 87.
- La Porta, A., Voth, G.A., Crawford, A.M., Alexander, J., Bodenschatz, E., 2001. Fluid particle accelerations in fully developed turbulence. *Nature*, 1017–1019.
- Lauga, E., Powers, T.R., 2009. The hydrodynamics of swimming microorganisms. *Rep. Prog. Phys.* 72 (9), 096601.
- Lazier, J.R.N., Mann, K.H., 1989. Turbulence and the diffusive layers around small organisms. *Sea Res. Part A: Oceanogr. Res. Pap.* 11 (36), 1721–1733.
- Locsei, J.T., Pedley, T.J., 2009. Run and tumble chemotaxis in a shear flow: the effect of temporal comparisons, persistence, rotational diffusion, and cell shape. *Bull. Math. Biol.* 71, 1089–1116.
- Lovely, P., Dahlquist, F.W., 1975. Statistical measures of bacteria motility and chemotaxis. *J. Theor. Biol.* 50, 477–496.
- MacKinnon, J., Gregg, M., 2003. Mixing on the late-summer New England shelf-solobores, shear, and stratification. *J. Phys. Oceanogr.* 33 (7), 1476–1492.
- Marwick, J.D., Wright, P.C., Burgess, J.G., 1999. Bioprocess intensification for production of novel marine bacterial antibiotics through bioreactor operation and design. *Marine Biotechnol.* 1, 495–507.
- Mopper, K., Lindroth, P., 1982. Diel and depth variations in dissolved free amino acids and ammonium in the Baltic Sea determined by shipboard HPLC analysis. *Limnol. Oceanogr.* 27 (2), 336–347.
- Munoz-Garcia, J., Neufeld, Z., Torney, C., 2010. Nutrient exposure of chemotactic organisms in small-scale turbulent flows. *New J. Phys.* 12 (10), 103043.
- Orszag, S.A., 1971. Numerical simulation of incompressible flows within simple boundaries: accuracy. *J. Fluid Mech.* 49 (1), 75–112.
- Paster, E., Ryu, W., 2008. The thermal impulse response of *Escherichia coli*. *Proc. Natl. Acad. Sci. USA* 105, 5373–5377.
- Pope, S.B., 2000. *Turbulent Flows*. Cambridge University Press edn., The Press Syndicate of the University of Cambridge.
- Rivero, M., Tranquillo, R., Buettner, H., Lauffenburger, D., 1989. Transport models for chemotactic cell populations based on individual behavior. *Chem. Eng. Sci.* 44 (12), 2881–2897.
- Rusconi, R., Guasto, J.S., Stocker, R., 1914. Bacterial transport suppressed by fluid shear. *Nature Phys.* 10 (3), 212–217.
- Schenk, P.M., Thomas-Hall, S.R., Stephens, E., Marx, U.C., Mussgnug, J.H., Posten, C., Kruse, O., Hankamer, B., et al., 2008. Second generation biofuels: high-efficiency microalgae for biodiesel production. *Bioenergy Res.* 1, 20–43.
- Seuront, L., 2008. Microscale complexity in the ocean: turbulence, intermittency and plankton life. *Math. Model. Nat. Phenom.* 3 (3), 1–41.
- Seymour, J., Marcos, R., Stocker, R., 2009. Resource patch formation and exploitation throughout the marine microbial food web. *Am. Nat.* 173 (E15).
- Smyth, W., Moum, J.N., 2000. Length scales of turbulence in stably stratified mixing layers. *Phys. Fluids* 12 (6), 1327–1342.
- Stocker, R., Seymour, J.R., 2012. Ecology and physics of bacterial chemotaxis in the ocean. *Microbiol. Mol. Biol. Rev.* 76 (4), 792–812.
- Stocker, R., et al., 2008. Rapid chemotactic response enables marine bacteria to exploit ephemeral microscale nutrient patches. *Proc. Natl. Acad. Sci. USA* 105 (11), 4209–4214.
- Stocker, R., 2012. Marine microbes see a sea of gradients. *Science* 338 (628).
- Taylor, J.R., Stocker, R., 2012. Trade-offs of chemotactic foraging in turbulent waters. *Science*. 338(6107), 675–679.
- Taylor, J.R., 2008. *Numerical Simulations of the Stratified Oceanic Bottom Boundary Layer* (Ph.D. thesis). University of California, San Diego, 2008.
- Tennekes, H., Lumley, J., 1972. *A First Course in Turbulence*. MIT Press.
- Williams, P., 2000. *Microbial Ecology of the Oceans*. Wiley-Liss, pp. 153–200.
- Yeung, P., Xu, S., Donzis, A.D., Sreenivasan, K.R., 2004. Simulations of three-dimensional turbulent mixing for Schmidt numbers of the order 1000. *Flow Turbul. Combust.* 72, 333–347.